Journal of Materials Chemistry A

REVIEW

View Article Online
View Journal | View Issue

Cite this: J. Mater. Chem. A, 2022, 10, 20218

Electronic structure engineering for electrochemical water oxidation

Pravin Babar,[abc] Javeed Mahmood,[abc] Raghu V Maligal-Ganesh,[abc] Seok-Jin Kim,[abc] Zhonghua Xue[abc] and Cafer T. Yavuz *[abc]

Received 17th June 2022
Accepted 10th September 2022

DOI: 10.1039/d2ta04833g

rsc.li/materials-a

The oxygen evolution reaction (OER) is the primary challenge in renewable energy storage technologies, specifically electrochemical water splitting for hydrogen generation. The development of affordable, robust, and efficient OER electrocatalysts plays a prominent role in water splitting by lowering the reaction kinetics barrier and boosting the performance of the process. This review discusses the recent progress in probing the electronic structure of catalytically active materials and its relevance to OER activity. We have aimed to emphasize state-of-the-art engineering strategies for modulating the electronic structure to exhibit ideal OER performance, including doping, alloying, generation of oxygen vacancies, heterostructure realization, and strain engineering. Finally, we summarize the existing challenges and opportunities in electronic structure modulation for future electrocatalyst development.

1. Introduction

Since the 19th century, fossil fuels such as coal, natural gas, and oil have become the primary energy source to sustain human activities.[1,2] The large-scale consumption of fossil fuels caused by unprecedented industrialization and rapid population growth, however, has resulted in detrimental environmental consequences and prompted the quest for more sustainable energy sources.[3–5] In this regard, rigorous efforts have been undertaken to shift the energy burden to renewable energy, such as those sourced from solar, tidal, and wind. The supply of energy from these sources, however, is intermittent and region/season dependent, hindering their widespread implementation.[6] To address this, renewable energy storage and conversion in the form of fuels and value-added chemicals is often proposed.[7] Among the candidates, hydrogen (H_2) is at the forefront, because it has a high gravimetric energy density and is environmentally benign.[8,9] But hydrogen is currently

[a]Oxide & Organic Nanomaterials for Energy & Environment (ONE) Lab, Physical Sciences and Engineering (PSE), King Abdullah University of Science and Technology (KAUST), Thuwal 23955, Saudi Arabia. E-mail: cafer.yavuz@kaust.edu.sa
[b]KAUST Catalysis Center, Physical Sciences and Engineering (PSE), King Abdullah University of Science and Technology (KAUST), Thuwal 23955, Saudi Arabia
[c]Advanced Membranes and Porous Materials Center (AMPMC), Physical Sciences and Engineering (PSE), King Abdullah University of Science and Technology (KAUST), Thuwal 23955, Saudi Arabia

Pravin Babar received his Ph.D. in Material Science and Engineering from the Chonnam National University, Korea, in February 2020. He is currently a Postdoctoral Researcher at the King Abdullah University of Science and Technology (KAUST), Saudi Arabia. His research interests include the development of transition-metal-based materials and their applications in electrochemical energy conversion systems, such as water splitting and nitrate reduction.

Javeed Mahmood is a Research Scientist at the Advanced Membrane & Porous Materials (AMPM) Center of King Abdullah University of Science and Technology (KAUST), Saudi Arabia. Before joining KAUST, he worked as a Research Assistant Professor at the Ulsan National Institute of Science and Technology (UNIST), South Korea. He received his Ph.D. from the School of Energy and Chemical Engineering at UNIST (South Korea) in 2015. His current research interests include design and synthesis of novel heterogenous catalysts and porous polymers for energy and environmental applications.

produced from steam reforming or partial oxidation of methane, or coal gasification. All these processes are fossil fuel based, with the added drawback that the purity of H_2 produced is also not high.[10] Not surprisingly, H_2 production through electrochemical water splitting has recently become an elegant and eco-friendly way to generate high purity H_2 at room temperature.[11–13]

Electrochemical water splitting is a thermodynamically uphill reaction, which consists of two half-cell reactions: the cathodic hydrogen evolution reaction (HER) and the anodic oxygen evolution reaction (OER) as described in eqn (1) and (2), respectively.[14]

$$\text{HER: } 2e^- + 2H^+(aq) \rightarrow H_2(g) \quad (1)$$

$$\text{OER: } 2H_2O(l) \rightarrow 4H^+(aq) + O_2(g) + 4e^- \quad (2)$$

In ideal reaction conditions, a thermodynamic potential of 1.23 V is needed to drive electrochemical water splitting. A practical water electrolyzer requires a much higher potential due to the overpotentials on both of the electrodes (anode and cathode).[15–17] HER is a comparatively simple two-electron transfer process involving adsorption of H^+ ions and desorption of H_2. OER, on the other hand, is more complicated, owing to sluggish oxygen evolution kinetics.[18,19] The OER is a four electron and proton coupled reaction with electron transfer occurring at each step of the four steps involving various reaction intermediates (*e.g.*, MOH, M–O, MOOH, and O_2) with oxygen produced as the final product (M is a catalytically active metal center).[20,21] Consequently, a large overpotential is required to overcome the OER kinetic energy barrier. Therefore, it is challenging to develop an efficient, cost-effective, and stable electrocatalyst for OER that can enhance the reaction rate and improve the overall efficiency of water splitting devices.

Over the past decade, numerous electrode materials have been developed and studied as electrocatalysts for OER. So far, the state-of-the-art IrO_2 and RuO_2 exhibit the best catalytic OER activity, but their low terrestrial availability and high cost limit their use in large scale applications.[22–24] Therefore, significant research has been directed toward developing earth-abundant transition-metal-based electrocatalysts including oxides, layered double hydroxides (LDH), nitrides, sulfides, selenides, and perovskite-based materials.[25–34] The transition-metal-based catalysts proved to have lower cost, higher natural abundance, unique electronic and mechanical properties, and good OER performances.[16,27,35,36] Despite the advances made so far on fabricating OER electrocatalysts with well-defined structures as well as *ex situ* characterizations, there is still room for

Dr Raghu V Maligal-Ganesh received his Ph.D. in Chemistry from Iowa State University, USA, in December 2017. Following his Ph.D., he worked as a Research Associate at Breathe Applied Sciences Pvt. Ltd and at the Jawaharlal Nehru Centre for Advanced Scientific Research (JNCASR), Bangalore. He is currently a Postdoctoral Researcher at the King Abdullah University of Science and Technology (KAUST), Saudi Arabia. His research interests focus on heterogeneous catalysis for sustainable chemistry initiatives.

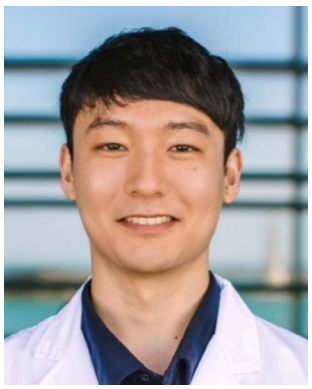

Seok-Jin Kim is a Postdoctoral Fellow at the Advanced Membrane & Porous Materials (AMPM) and KAUST Catalysis Center (KCC) of King Abdullah University of Science and Technology (KAUST) in Saudi Arabia. He received Ph.D. from the School of Energy and Chemical Engineering at Ulsan National Institute of Science and Technology (UNIST), South Korea, in 2019. His current research focus is on improving catalytic activity based on material science.

Zhonghua Xue received his Ph.D. in Chemistry from Shanghai Jiao Tong University, China, in March 2020. He is currently a Postdoctoral Researcher at the King Abdullah University of Science and Technology (KAUST), Saudi Arabia. His current research focuses mainly on designing and fabricating efficient catalysts for electrochemical reactions (e.g., water splitting and N_2/CO_2 reduction).

Cafer T. Yavuz is currently a Professor of Chemistry at King Abdullah University of Science and Technology (KAUST), Saudi Arabia. He received his Ph.D. degree from Rice University. His current research is focused on the design and making of new nanomaterials from oxide or organic building blocks to offer sustainable solutions for the pressing issues such as carbon dioxide capture, water treatment, and catalysis.

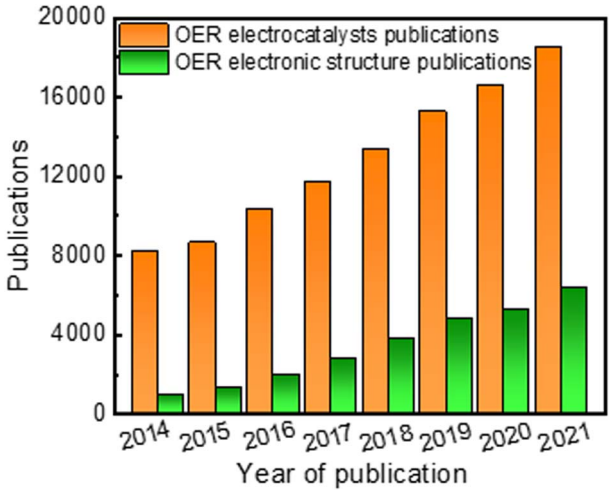

Fig. 1 Summary of the literature for OER electrocatalysts from Web of Science. Bar chart of the number of articles published per year from 2014 to 2021 on OER (orange bars) and those related to electronic structure modulation (green bars). The data for OER were obtained by searching the keywords "oxygen evolution reaction" or "water splitting" or "electrocatalyst". The data for electronic structure modulation were obtained by adding "electronic structure" or "electronic structure modulation" as the keywords.

improvement in the electrochemical activity and stability of transition metal-based catalysts.

Apart from material type, several strategies have been explored to enhance electrocatalytic performance, including chemical composition tuning,[19] morphology and phase control,[37] defect engineering,[38] and electronic structure modulation.[16] Generally, the most basic structural characteristics, such as specific surface area and porous microstructure of the catalyst, have been studied as the key parameters for improving electrochemical performance for OER. For instance, the mass transfer rate and the number of active sites have been substantially enhanced in high surface area catalysts like 3D structures, 2D nanosheet structures, 1D nanorod/nanowire structures, and 0D nanoparticles.[37,39] Despite extensive efforts in synthetic tuning, improvements in electrochemical performance of great significance are challenging to attain. This is because the overall electrocatalytic performance of a catalyst is often governed by its electronic structure, more than anything else. In the past few years, research dabbling in electronic structure modulation to overcome the sluggish kinetics of OER has steadily gathered steam (Fig. 1). For example, in 2014 there were more than 8100 papers on the topic of OER electrocatalysts, among them around 930 papers pay specific attention on strategies to modulate electronic structure. A few recent review and perspective articles summarized the development of noble and non-noble metal-based OER electrocatalysts with an emphasis on a given synthetic methodology or a specific electronic structure modulation strategy or classes of materials that can improve OER performance.[40–42] However, there is a lack of an overall understanding and explanation of the relationship between electrochemical properties and electronic structure towards the development of electrocatalysts for water splitting applications. Therefore, we believe our review is a timely and critical overview of recent progress in the electronic structure modulation of electrocatalysts for enhanced OER performance.

In this review, we summarize key advances in regulating the electronic structure of electrocatalytic materials for enhanced OER. We have identified the best electronic structure modulation methods as doping, alloying, oxygen vacancy generation, heterostructure, and strain engineering (Fig. 2). These approaches tune the electronic structure and improve the OER performance. We have included a detailed discussion on how the respective electronic structure tuning strategies can lead to enhanced OER activity. Such strategies provide new insights into the design and construction of an efficient electrocatalyst. Finally, we have discussed some existing challenges in these efforts and provided recommendations for future research directions.

2. Fundamentals of oxygen evolution reaction (OER)

One of the main reasons that limit water splitting systems from being practical is the sluggish kinetics of the OER. The OER is

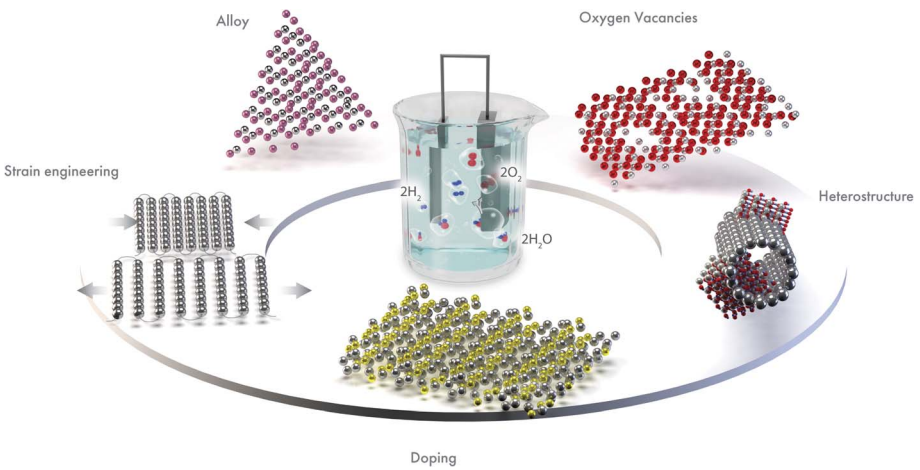

Fig. 2 Leading electronic structure modulation strategies for best OER performance.

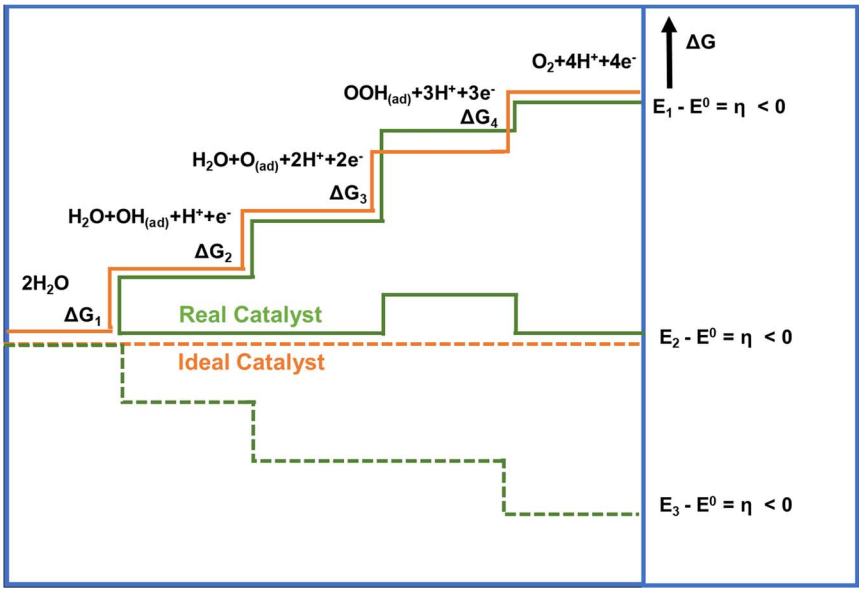

Fig. 3 Gibbs free energy plot of OER *versus* reaction coordinate for the reactive intermediates (horizontal lines), the energetics of a real catalyst and an ideal catalyst has been represented by orange and green lines respectively.[45] Copyright 2010, Wiley-VCH.

a four-electron transfer process which increases the complexity of the overall electrolysis, and requires higher energy to overcome the kinetic barrier.[43] It is favorable in an alkaline electrolyte when compared to neutral or acidic media. In the acidic or neutral electrolyte, the free hydroxyl groups (OH) are absent, so the generation of OH* by breaking the H–OH bond from water molecules has a high energy barrier for the OER initiation. It results in slow OER kinetics while drawing high overpotential. The Gibbs free adsorption energies (ΔG) in the four-electron transfer step are shown in Fig. 3. The process involves (i) adsorption of H_2O at the catalyst surface, (ii) formation of reaction intermediates from H_2O ($OH_{(ad)}$, H^+, e^-), (iii) conversion of $OH_{(ad)}$ to $O_{(ad)}$, along with the generation of an additional proton and electron (iv) formation of the O–O bond *via* $OOH_{(ad)}$, an additional proton and an electron, and lastly (iv) desorption of oxygen from the catalyst surface, accompanied by the release of an additional proton and electron, with the overall process involving the total release of 4 protons and 4 electrons.[44] For an ideal catalyst, the Gibbs free energy for every elementary step should be equal ($\Delta G_1 = \Delta G_2 = \Delta G_3 = \Delta G_4$), but in the case of the real catalysts, the chemisorption energy of the intermediates follow the order: $\Delta G_3 > \Delta G_1 = \Delta G_2 > \Delta G_4$.[45,46]

As mentioned above, OER involves the formation of high-energy intermediates, requiring a substantial amount of energy to transcend the free energy barrier.[47,48] Therefore, electronic structure modulation of catalytic materials is necessary to overcome these kinetic barriers, ensuring favorable reaction pathways with optimum free energy changes for the adsorption of the reaction intermediates at the catalyst surface. The ensuing strategies to achieve electronic structure modulation help in beneficial changes to adsorption energy that lower these kinetic barriers. These aid in reducing the overpotential of OER for these modified catalysts, attempting to bring it closer to that for an ideal catalyst (1.23 V).

3. Electronic structure modulation strategies for the OER electrocatalysts

3.1. Doping

Doping electrocatalysts have been reported as the most effective method to modulate electronic structure at the atomic level, which helps to improve water dissociation and optimize the adsorption capacity for the reaction intermediates. It generates lattice defects, which enhances the amount of available active sites in an electrocatalyst. Doping metal atoms (single metal or multimetallic) into transition metal-based catalysts such as layered double hydroxides (LDH), oxides, or chalcogenides serve as a promising strategy for enhancing the electrochemical activity.[25,49,50] Due to the variation in the atomic radii and the electronic configuration of the dopant, the original lattice is likely to be altered and induced a local electronic redistribution. Moreover, doping may increase the adsorption energy of reaction intermediates because of the change in electronic structure. Many reports demonstrated that metal doping successfully improved catalytic performance.[16,51–54] Among these, Fe incorporation is frequently established in that it enhances the electrochemical OER performance of Ni and Co-based catalysts.[18,55] In the early 1980s, studies by Corrigan[56] and Młynarek *et al.*[57] found that Fe impurities enhance the OER performance. After these groundbreaking studies, Boettcher *et al.* further verified this argument by preparing NiO_x, CoO_x, $Ni_yCo_{1-y}O_x$, $Ni_{0.9}Fe_{0.1}O_x$, IrO_x, MnO_x, and FeO_x films of 2–3 nm thickness using a solution casting method.[58] They found that $Ni_{0.9}Fe_{0.1}O_x$ was the best catalyst with lower overpotential and also a lower Tafel slope. The enhancement of OER activity was attributed to the *in situ* formation of a layered double hydroxide (LDH) structure, which has more active sites than metal oxide or hydroxide. The same group also reported the effect of Fe incorporation in $Ni(OH)_2$/NiOOH during the OER.[49] A 30-fold increase in catalyst

conductivity accompanied by the formation of the LDH phase was observed when Fe was incorporated into $Ni(OH)_2$. Electrochemical results show an anodic shift of Ni redox peaks in $Ni_xFe_{1-x}OOH$ catalysts with increasing x.

Advanced spectroscopic techniques provide further insight into what addition of a dopant into these various catalysts achieves. Friebel and co-workers[50] used X-ray absorption spectroscopy (XAS) using high energy resolution fluorescence detection (HERFD) to reveal the role of Fe^{3+} in a $Ni_{1-x}Fe_xOH$ based electrocatalyst. A key finding was that Fe^{3+} in NiFeOH occupies octahedral sites with short Fe–O bond distance induced by edge-sharing with surrounding $[NiO_6]$ octahedra. Further computational calculations identified that Fe cations were the active sites instead of Ni in mixed Fe–Ni oxyhydroxide. Similar findings have been reported for Fe doped Co-based electrocatalysts,[18,19,59] which suggest that Fe incorporation has a promoter influence on Co and Ni-based catalysts. Using Mössbauer spectroscopy[60] Jamie and co-workers revealed[61] that Fe in an NiFe LDH existed as Fe^{4+} and was not the active site of the catalyst and instead functioned as an effective dopant to drastically enhance the OER performance of the Ni atoms. Görlin *et al.* used differential electrochemical mass spectrometry (DEMS) and X-ray absorption spectroscopy (XAS)[62] to indicate that Ni in pure NiOOH electrode changes redox state from Ni^{2+} to Ni^{3+} or Ni^{4+} during the OER process, while in a mixed Ni–Fe electrocatalyst, Ni remains in the Ni^{2+} state, which might be responsible for the enhancement of the catalytic performance (Fig. 4a and b). Zhang and co-workers showed enhancement in the OER performance of NiO by Li doping, which could be due to electronic structure modifications.[63] The results revealed that generation of hole states at 1.1 eV above the Fermi level and enlarged hybridization degree of O 2p–Ni 3d by Li-doping optimize the adsorption energies of OH intermediates (Fig. 4c).[63]

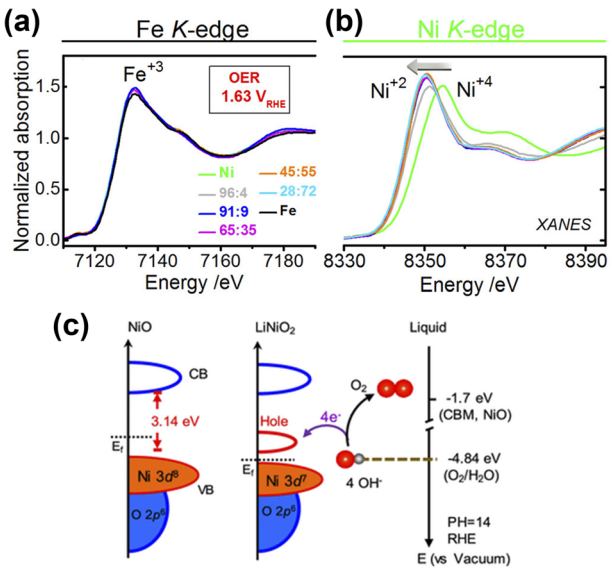

Fig. 4 X-ray absorption spectra and electronic structure analysis of electrocatalysts (a) X-ray absorption spectrum of Fe K-edges and (b) Ni K-edges.[62] Copyright 2017, American Chemical Society (c) schematic diagram for electronic structures of NiO and $LiNiO_2$ (left) and energy diagram at the oxide–liquid interface on the vacuum level scale at pH = 14 (right); the redox level for O_2/H_2O (red dashed line) is −4.84 eV, the CB minimum (CBM) level for NiO is −1.7 eV according to the formula: $E_{CBM} = E_{bandgap} - E_{ionization}$, ($E_{bandgap}$ = 3.7 eV, $E_{ionization}$ = 5.4 eV).[63] Copyright 2017, American Chemical Society.

A key aspect of doping metal atoms into pristine materials is the effect this has on the density of states at the Fermi level, with potential benefits for their catalytic behavior. Li and co-workers showed Co doping in Cu_7S_4 enhances the OER performance due to the optimized electronic structure of active sites.[64] The calculated density of states (DOS) for Co-doped Cu_7S_4 is closer to the Fermi level than that of pristine Cu_7S_4, indicating that the concentration of charge carrier and the electronic conductivity can be effectively enhanced by the introduction of Co atoms. The Co-doped Cu_7S_4 improved OER performance even at a low overpotential of 270 mV to reach 10 mA cm^{-2}. Wang *et al.* showed that nitrogen doping could regulate adsorption sites in the nanostructured ultrathin CoFe LDHs.[65] Nitrogen doping redistributes the electron density of adjacent Co or Fe atoms, which optimize the adsorption energy of OER intermediates, thus enhancing electrocatalytic performance. Based on the theoretical analysis, Niu *et al.* showed that doping FeOOH with selenium (Se) lowers the energy barrier for the OER rate-limiting step and also enhances intrinsic activity.[66]

Doping or substituting transition metals in spinel metal oxides has also become an effective way to tune the electronic structure and enhance the OER performances of these versatile materials. Recently, doping spinel-based Co_3O_4 with Ni, Cu, Zn and Fe has been widely reported, and their effect on the electronic structure and electrochemical behavior have also been investigated.[25,67–69] In the case of the Zn–Co spinel structure, Zn substitutes the Co^{2+} in tetrahedral sites and Co^{3+} remains in the octahedral sites. The enhancement in OER performance of $Zn_xCo_{3-x}O_4$ compared to Co_3O_4 emerges from the altered electronic and structural nature of substituted tetrahedral sites. Choi and co-workers prepared spinel-type $ZnCo_2O_4$ and Co_3O_4 electrocatalysts to show these effects.[70] The results suggest that $ZnCo_2O_4$ has better OER performance (η = 390 mV at 10 mA cm^{-2}) than Co_3O_4 (η = 450 mV at 10 mA cm^{-2}), which may be due to Co^{2+} in Co_3O_4 being catalytically inactive. Driess and co-workers reported the superior efficiency of $ZnCo_2O_4$ electrocatalyst to that of Co_3O_4 for the OER.[71] The reason for the better catalytic activity was attributed to a higher amount of accessible octahedral Co^{3+} sites induced by preferential loss of zinc ions from the surface of the $ZnCo_2O_4$ electrocatalyst. Further, Xu and co-workers did a systematic study of spinel $ZnFe_xCo_{2-x}O_4$ oxides (x = 0–2.0) for the OER.[72] The enhanced OER performance is attributed to enlarged Co 3d and O 2p covalency brought about by 10–30 atom% Fe substitution as it facilitates the injection/extraction of electrons from oxygen (Fig. 5a and b).

Previous studies showed the significance of pre-oxidation of Co^{2+} to Co^{3+} or higher oxidation states in generating active sites of Co–OOH for OER.[73] Papakonstantinou *et al.* synthesized $CuCo_2O_4$ nanoparticles (4.0 nm size) and anchored these on nitrogenated reduced graphene oxide ($CuCo_2O_4$/NrGO).[74] The $CuCo_2O_4$/NrGO catalyst demonstrated enhanced OER performance due to the presence of Cu^{2+} ions at octahedral sites.

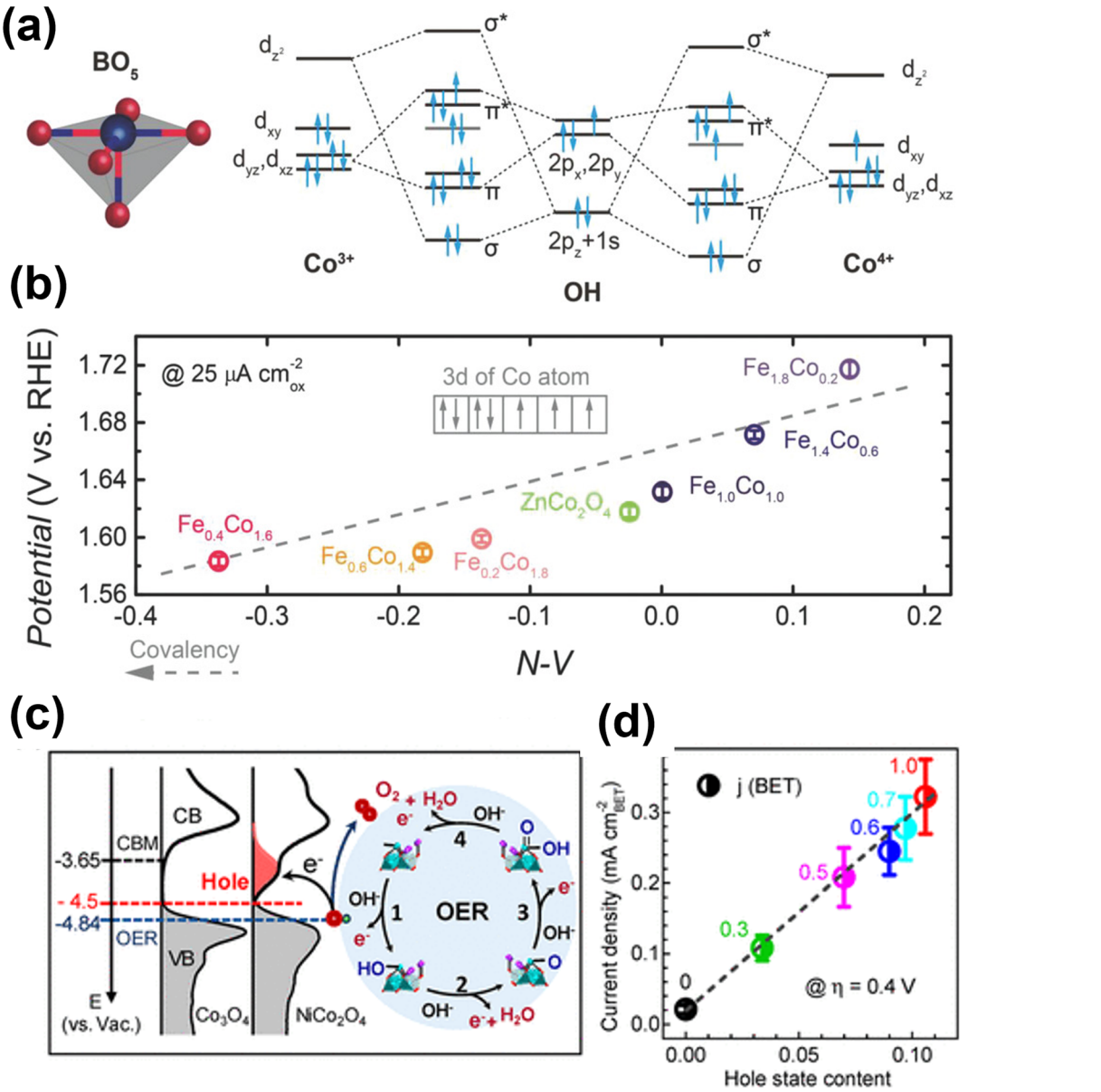

Fig. 5 Performance and computational studies of oxide based OER electrocatalysts (a) molecular orbitals diagrams for the Co–OH (Co^{3+}, Co^{4+}) bonding at the surface of spinel oxides. (b) The OER activity, evaluated by the potentials at a current density of 25 μA cm_{ox}^{-2}, as a function of the *N–V* parameter.[72] Copyright 2018, Wiley-VCH. (c) Left panel: the measured occupied and unoccupied density of states (DOS) near the EF for Co_3O_4 and $NiCo_2O_4$; the energy level is relative to vacuum level (*vs.* V_{ac}); the redox level for O_2/H_2O (blue line) is −4.84 eV; the hole state level is −4.5 eV for $NiCo_2O_4$ and the CBM level for Co_3O_4 is −3.65 eV. Right panel: schematics of the four-step reaction pathway of OER. (d) Correlation of specific OER activity (current density at $\eta = 0.4$ V) with the amount of hole state extracted from O K edge XAS spectra.[76] Copyright 2019, American Chemical Society.

Recently, Pentcheva and co-workers theoretically investigated the effect of Fe and Ni doping on Co_3O_4 (001) surface for the OER.[75] The results suggest that the Ni doping at the octahedral site on the surface layer reduces the η from 0.46 to 0.34 V. Similarly, Fe doping at the tetrahedral Co termination lowers η from 0.63 to 0.37 V with octahedral Co remaining in the active site. Zhang and co-workers systematically studied the relationship between electronic structure and the OER activity of Ni_x-$Co_{3-x}O_4$ ($x = 0$–1).[76] The XPS analysis reveals that incorporation of Ni^{3+} ions shifts the occupied valence band maximum by 0.27 eV towards the Fermi level (E_F) and generates a new hole (unoccupied) state located at ~1 eV above E_F, which reduces the energy barrier for electron transfer to enhance the kinetics (Fig. 5c and d).

Incorporating more than one element to enhance the electrochemical performance of the electrocatalyst is garnering significant research scrutiny. Tang and co-workers developed Co and Ce doped Ni_3S_2 (Co/Ce-Ni_3S_2/NF) nanosheets on nickel foam by a one-step hydrothermal method.[77] The co-doped Co and Ce are uniformly distributed inside the host sulfide,

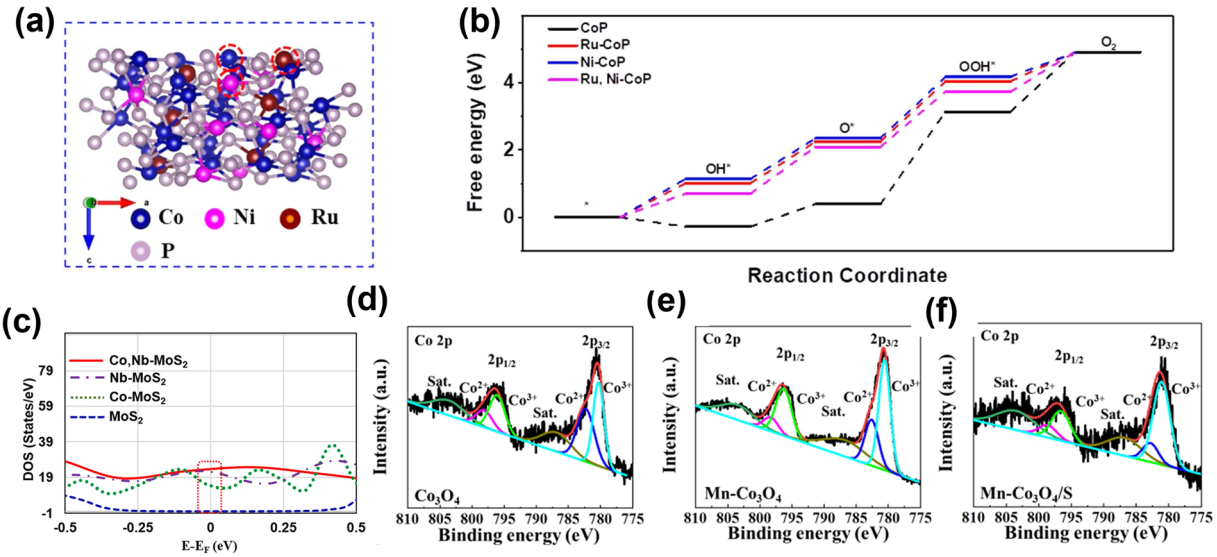

Fig. 6 The role of double atom doping in OER electrocatalysts. (a) Atomic structure of Ru, Ni-CoP (111) surface, where Co, Ni, and Ru sites are marked with red circles. (b) Calculated OER Gibbs free energy diagram for CoP, Ru-CoP, Ni-CoP, and Ru, Ni-CoP.[79] Copyright 2021, Elsevier. (c) Calculated DOS curves for MoS_2, Co-MoS_2, Nb-MoS_2 and Co, Nb-MoS_2.[80] Copyright 2021, Elsevier. Co 2p spectra in (d) Co_3O_4, (e) Mn-Co_3O_4, and (f) Mn-Co_3O_4/S.[81] Copyright 2019, Elsevier.

providing more active sites and increasing electrical conductivity. The incorporation of metallic elements into Ni_3S_2 has been considered as an effective strategy to alter the electronic structure to a disordered state, which increases the density of states (DOS). The DFT calculations further revealed that Ni_3S_2 displayed more metallic states near the Fermi level after Co and Ce doping, with the electronic conductivity being significantly increased and electron transport accelerated. Using a simple hydrothermal method, Wang *et al.* reported highly active Ru and Ni co-doped Co_3O_4 (Ru/Ni-Co_3O_4) nanoparticles.[78] Doping Ru atoms into octahedral sites of spinel oxide Co_3O_4 improves the intrinsic activity, while Ni creates abundant oxygen vacancies. By demonstrating high intrinsic activity and the exposure of more active sites, the optimized Ru/Ni-Co_3O_4 shows a low overpotential for OER (290 mV at 10 mA cm^{-2}). Similarly, Cheng and colleagues[79] prepared Ru and Ni dual-doped CoP (Ru, Ni-CoP) porous nanofibers. Dual metal-doping (Ru and Ni) can modulate the electronic structure compared to single metal-doping. The Ru, Ni-CoP exhibit low free energy of 1.65 eV compared to Ru-CoP (1.80 eV) and Ni-CoP (1.83 eV) (Fig. 6a and b), revealing a higher adsorption capacity for *OOH. This enhanced adsorption capacity results from the higher valence state of Co caused by dual-metal doping. Recently, Kim and colleagues prepared Co, Nb dual-doped MoS_2 nanosheets on TiO_2 hollow spheres (Co, Nb-MoS_2/TiO_2 HSs), wherein the synergy between the hollow spherical structure of the TiO_2 core and the MoS_2 shell was exploited for enhanced electron transfer.[80] Additionally, the Co and Nb doping further modified the electronic structure of the MoS_2 to boost the OER performance. As shown in (Fig. 6c), DOS results indicate the electronic state of Co, Nb-MoS_2/TiO_2 HSs is closer to the Fermi level and higher than its counterparts, thus facilitating easier electron transfer and enhancing the adsorption of the intermediates. Qi and co-workers synthesized nanosheets of Co_3O_4 co-doped with both Mn and S that exhibited enhanced OER activity in comparison to the pristine Co_3O_4 nanosheets or Co_3O_4 doped only with either Mn or S.[81] While Mn doping modifies the electronic structure around the Co center, enhancing the intrinsic activity of the active sites in Co_3O_4. On the other hand, S doping provides abundant S sites for proton desorption and increases the electrical conductivity. Furthermore, an increase in the proportion of Co^{3+} sites is also observed (Fig. 6d–f), which facilitates the four-electron transfer and the enhanced OER performance.

3.2. Oxygen vacancy engineering

The introduction of oxygen vacancies in metal oxide nanomaterials is one of the most effective techniques to regulate their chemical and electronic characteristics. Oxygen vacancies improve the electrocatalytic performance *via* the enhancement of the synergy between the active sites and the neighboring atoms to enhance the DOS near the Fermi level.[6] This further accelerates the electron transfer rate and instability of the metal–oxygen bond. Additionally, oxygen vacancies positively improve OER performance by significantly altering the energy level, conductivity, and adsorption properties of the materials. Various synthetic methods were used to generate oxygen vacancies, such as thermal treatment, reduction by $NaBH_4$,[82,83] ion exchange, plasma treatment,[84,85] doping of ionic liquid,[86] and *in situ* electrochemical activation.

3.2.1. Reduction approach. Oxygen vacancies can be formed in nanomaterials using $NaBH_4$ as the reducing agent in the liquid phase. The $NaBH_4$ reduces the metal ions of the metal oxide in aqueous media according to the following equation:[87]

$$8M^{n+} + NaBH_4 + 2H_2O \rightarrow 8M^{(n-1)+} + NaBO_2 + 8H^+$$

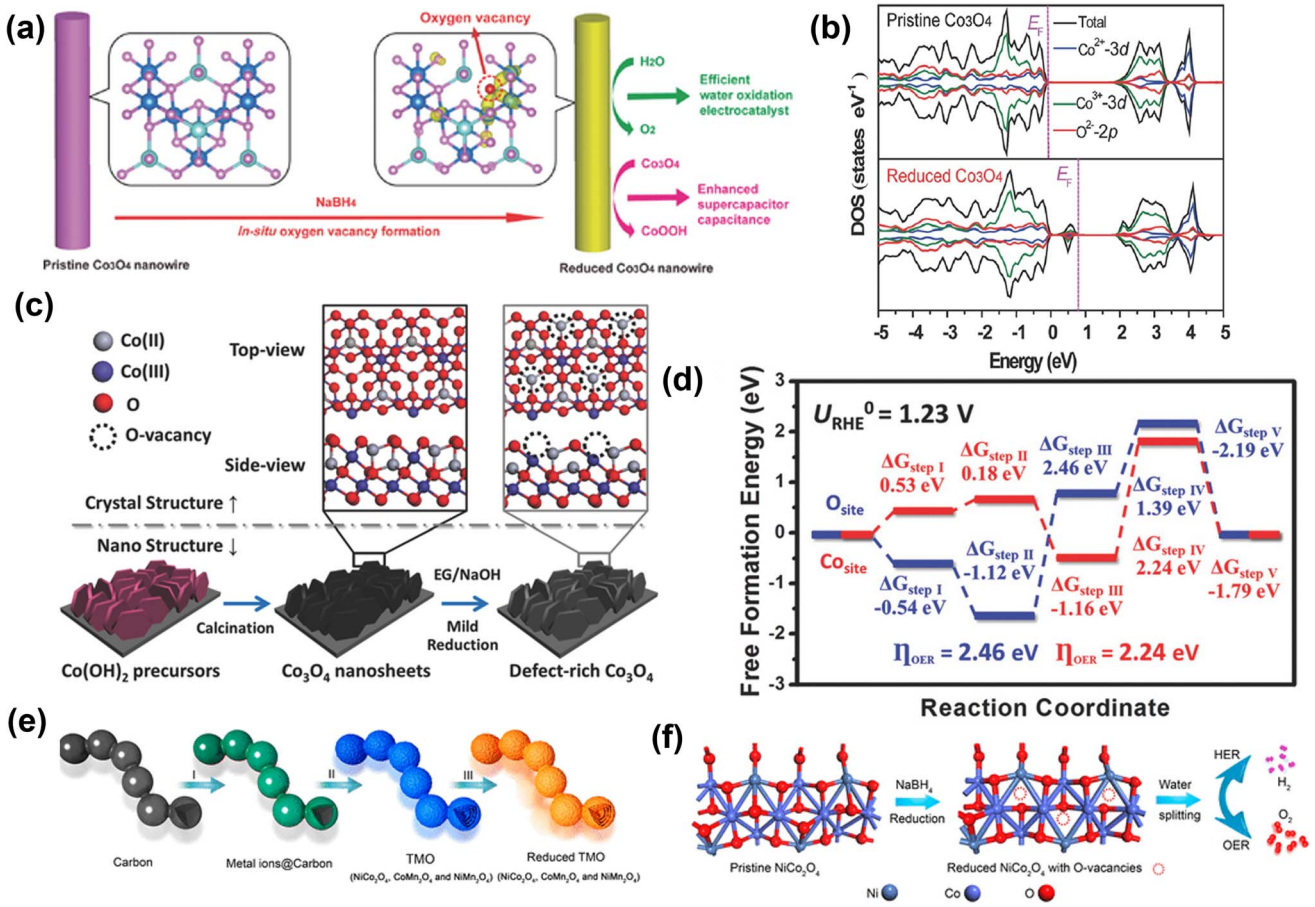

Fig. 7 Reduction approach for vacancy generation in OER catalysts. (a) Schematic of the $NaBH_4$ reduction for *in situ* creation of oxygen vacancies in Co_3O_4 NWs for efficient catalysis of oxygen evolution reaction and enhanced supercapacitor capacitance, (b) total densities of states (TDOS) and projected densities of states (PDOSs) of the pristine Co_3O_4 and the reduced Co_3O_4 (with oxygen vacancies).[88] Copyright 2014, Wiley-VCH. A new state is formed within the bandgap of the reduced Co_3O_4. (c) Schematic illustration of creating oxygen vacancy defects on the surface of single-crystalline ultrathin Co_3O_4 nanosheets. The pristine Co_3O_4 nanosheets were grown directly on Ni foam substrate, then mildly reduced by ethylene glycol (EG) under alkaline condition, introducing, oxygen vacancy defects on the O-terminated {111} facets of single-crystalline Co_3O_4 nanosheets. (d) The calculated OER free energy diagram of the Co_3O_4 structure with/without oxygen vacancy.[89] Copyright 2018, Wiley-VCH. (e) Schematic illustration of the formation process of R-TMO with a necklace-like multi-shelled hollow structure for water splitting. (f) Schematic illustration of creating oxygen vacancy defects on the surface of NCO after reduction, which is applied as a bifunctional electrocatalyst for water splitting to produce H_2 and O_2 in 1.0 M KOH aqueous solution.[90] Copyright 2018, American Chemical Society.

Zheng and co-workers prepared 1D Co_3O_4 nanowires with rich oxygen vacancies using the $NaBH_4$ reduction method.[88] To prepare Co_3O_4 nanowires, they used a wet chemical growth method, and then as-prepared Co_3O_4 nanowires were soaked in 1 M $NaBH_4$ solution for 1 h (Fig. 7a). After $NaBH_4$ treatment, oxygen vacancies were created in Co_3O_4 nanowires and confirmed by XPS analysis. The DFT analysis revealed that due to oxygen vacancies, new defect states are generated and located in the band gaps (Fig. 7b). In addition, calculated formation energy suggests that the electrons at the oxygen vacancy defects can be easily excited into the conduction band, enhancing conductivity and the electrochemical activity of Co_3O_4 with a lower value of onset potential (1.52 V *vs.* RHE).

Sun and co-workers used a solvothermal reduction approach to create oxygen defects in single-crystalline Co_3O_4 nanosheets, as shown in Fig. 7c.[89] The defect-rich Co_3O_4 shows a lower overpotential of 220 mV with a lower Tafel slope of 49.1 mV dec^{-1} for OER. Furthermore, the DFT calculation indicates a lower OER activation energy value of 2.24 eV on oxygen vacancy-rich Co_3O_4 than the pristine Co_3O_4 (2.46 eV) (Fig. 7d). Peng *et al.* prepared a unique necklace-like multi-shelled hollow structure of spinel transition metal oxides ($NiCo_2O_4$ (NCO), $CoMn_2O_4$, and $NiMn_2O_4$) using an adsorption–calcination–reduction strategy (Fig. 7e and f).[90] The DFT calculations reveal a mechanism for enhancing catalytic performance based on a decrease in energy barrier for the formation of intermediates due to the introduction of oxygen vacancies. Zho and co-workers showed that an oxygen vacancy-rich NiFe-based catalyst yields a more than 2-fold increased current density at a low overpotential (370 mV @ 31 mA cm^{-2}) in comparison to the pristine catalyst (370 mV @ 15 mA cm^{-2}).[91] Further, Zhu and co-workers used the reduction method to prepare ultrathin iron–cobalt oxide nanosheets (Fe_xCo_y-ONSs) with abundant oxygen vacancies as OER electrocatalysts.[92] The Fe_xCo_y-ONSs showed excellent OER activity due to rich oxygen vacancies that could

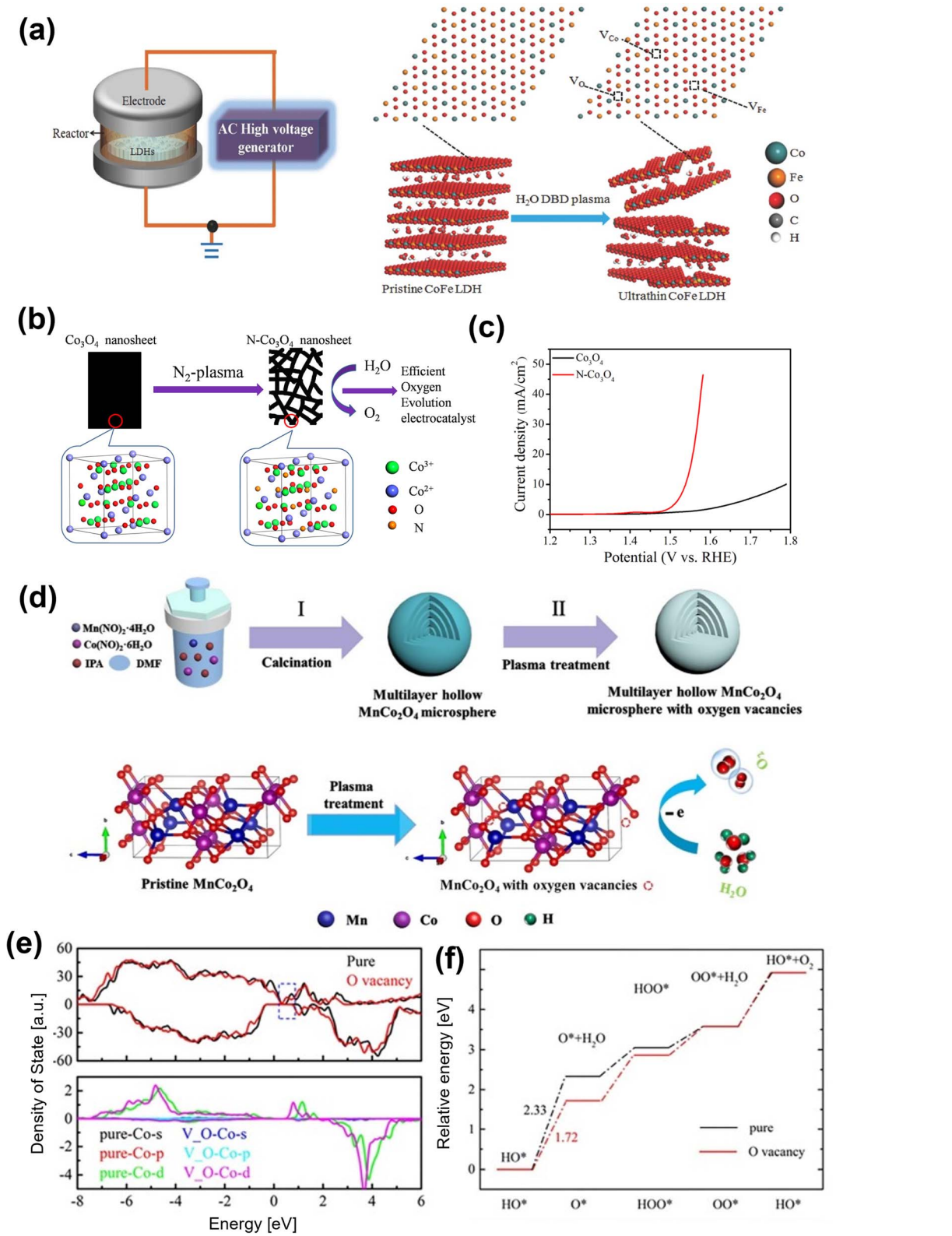

Fig. 8 Plasma treatment for oxygen vacancy generating in OER electrocatalysts (a) schematic illustration of the water-plasma-enabled exfoliation of CoFe LDH nanosheets. The DBD plasma reactor is designed with the plate-to-plate electrode at 50 V powered by the AC high voltage generator.[98] Copyright 2017, Wiley-VCH. (b) Schematic illustration of the preparation of the N-doped and etched Co_3O_4 nanosheets, (c) the polarization curves of the OER on pristine Co_3O_4 nanosheets and the N-doped Co_3O_4 nanosheets.[101] Copyright 2017, IOP Publishing. (d) Illustration of the preparation of multilayer hollow $MnCo_2O_4$ microsphere (pristine $MnCo_2O_4$) and the introduction of oxygen vacancies (Vo-$MnCo_2O_4$). (e) The calculated density of states for $MnCo_2O_4$ (0 0 1) with and without oxygen vacancies (upper panel) and density of states projected on the surface Co atom (lower panel). (f) The energy profile for the OER process on $MnCo_2O_4$ with and without oxygen vacancies at zero potential.[102] Copyright 2021, Elsevier.

improve electronic conductivity and facilitate the adsorption of H_2O onto nearby Co^{3+} sites.

3.2.2. Thermal treatment. The most common approach to generating oxygen vacancies in metal oxides is to anneal the metal oxides at elevated temperatures under inert or reduced pressure conditions. The oxygen vacancy concentration can be tuned by adjusting inert gas flow rate during annealing or processing temperature.

Xie and colleagues successfully synthesized ultrathin nanosheets of the $NiCo_2O_4$ spinel with oxygen deficiencies by calcination of NiCo hydroxide in air at 300 °C.[93] These ultrathin $NiCo_2O_4$ nanosheets with rich oxygen vacancies exhibited a high current density of 285 mA cm^{-2} at 0.8 V *vs.* Ag/AgCl. The theoretical calculations showed that oxygen vacancies confined in the ultrathin nanosheets could lower the adsorption energy of H_2O, which enhances the OER efficiency. Cheng *et al.* have demonstrated that the electrocatalytic activity of MnO_2 is boosted by generating oxygen deficiencies.[94] The MnO_2 with oxygen vacancies were prepared by simply heating in air or Ar atmosphere. Surprisingly the MnO_2 samples heated in Ar (350 °C) and air (400 °C) outperformed the other samples that were annealed at the same temperatures but for longer durations. Hence generating an optimum concentration of oxygen vacancies was crucial wherein these oxygen vacancy enriched MnO_2 samples showed a large current and lower overpotential. DFT study reveals that oxygen vacancies enhance the interaction between MnO_2 surfaces and oxygen-containing species, and therefore reduce the kinetic barrier. Shi and co-workers successfully generated two different oxygen vacancy concentrations ($\delta = 0.25$ and 0.50) in a perovskite oxide ($PrBaCo_2O_{6-\delta}$) by annealing under pure N_2 atmosphere for 30 min at 250 and 600 °C, respectively.[95] They found that when oxygen vacancies were increased to $\delta = 0.50$, the OER activity is reduced significantly. The reduced OER performance may be due to a significant reduction in e_g filling of Co ions, which increases the electric resistivity and weakens the Co–O bond covalency. These results indicate that an optimal oxygen vacancy loading should be investigated for the high OER activity of any candidate materials.

3.2.3. Plasma treatment. Oxygen vacancies can be created on the surface of the electrodes by exposing them to high-energy ion (N_2^+, Ar^+, H_2O^+) bombardment. A plasma is a partially ionized gas and includes ions, electrons, radicals, photons, molecules, and excited species, which remove oxygen from the surface to produce oxygen vacancies.[96] The oxygen vacancies created by plasma treatment are conducive to modulate the electronic structures, providing rapid electron transfer, and enhancing the electrochemical performance.[97] Liu *et al.* prepared CoFe LDH nanosheets with oxygen vacancies by water-plasma-enabled exfoliation.[98] Fig. 8a shows the experimental set-up of the dielectric barrier discharge (DBD) plasma reactor for creating the oxygen vacancies in CoFe LDH by partially etching the interlayer anions. The vacancies in CoFe LDH nanosheets show a positive effect in enhancing the electrocatalytic OER activity of CoFe LDH nanosheets. Similarly, Hou and co-workers developed an oxygen vacancy-rich NiFe-LDH electrocatalyst by water-plasma-assisted synthesis.[99] The

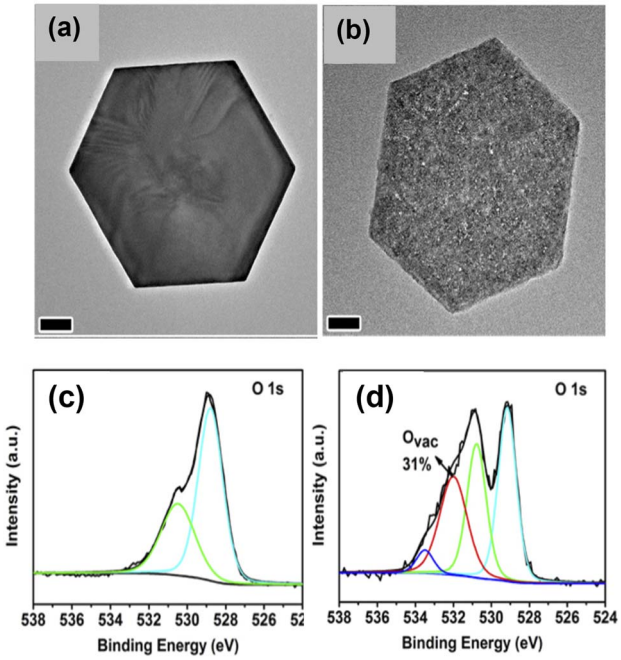

Fig. 9 Ligand-assisted reduction method to generate oxygen vacancies on cobalt oxide nanoplates. TEM images of (a) α-$Co(OH)_2$ and (b) CoO_x. O 1s XPS spectra of (c) CoO-cal, and (d) CoO_x.[111] Copyright 2018, Elsevier.

oxygen-enriched NiFe-LDH nanosheets possessed a large petal-like structure (~3 μm) and high BET surface area, which is favorable for enhancing the catalytic performance for OER.

Zhi and co-workers adopted the Ar plasma strategy to introduce oxygen vacancies to Co_3O_4 and produced Co_3O_{4-x}.[100] The oxygen vacancy-rich Co_3O_{4-x} promoted the reversible Co–O ↔ Co–O–OH redox reaction and lead to an enhancement in OER performance. Xu *et al.* prepared an efficient Co_3O_4 electrocatalyst for electrocatalytic OER with oxygen vacancies by a one-step Ar plasma-engraving strategy.[85] The Co 2p XPS analysis reveals that in comparison to pristine Co_3O_4, the plasma-engraved Co_3O_4 surface has more Co^{2+} oxidation states, suggesting a partial reduction of Co^{3+} ions to Co^{2+} with the creation of oxygen vacancies on the Co_3O_4 surface. The Co_3O_4 nanosheets with oxygen vacancies significantly increased the surface area and the specific activity, resulting in better OER activity. The same group also reported N-doped nonporous Co_3O_4 nanosheets with oxygen vacancies by N_2 plasma as an efficient OER electrocatalyst (Fig. 8b).[101] An increase in active sites owing to the generated oxygen vacancies leads to higher electronic conductivity, resulting in excellent electrocatalytic activity with a lower overpotential of 310 mV at 10 mA cm^{-2} (Fig. 8c). Yang and co-workers recently used the plasma-engraving technique to create oxygen vacancies in multilayered $MnCo_2O_4$ microspheres (Fig. 8d).[102] The defective $MnCo_2O_4$ increases the number of exposed active sites and promotes OER kinetics, further enhancing OER performance. Theoretical calculations confirm that the introduction of oxygen vacancies in $MnCo_2O_4$ can reduce the DOSs near the Fermi level and lower the Co d-band center, weakening the adsorption intermediates (Fig. 8e and f).

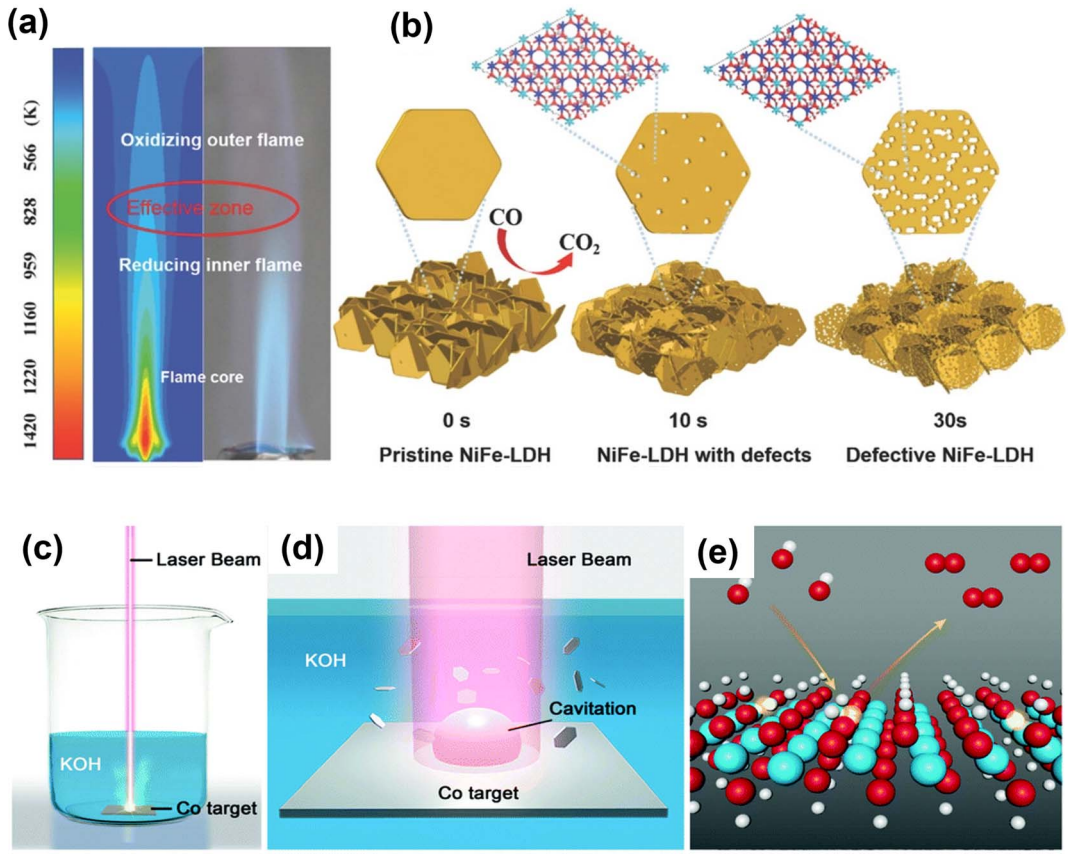

Fig. 10 Schematic illustration of defective NiFe-LDH and L-CoOOH with oxygen vacancies prepared by fast reducing flame treatment and laser ablation in liquid for creating oxygen vacancies in transition-metal oxides. (a) Temperature distribution simulation of flame. (b) Morphology change of NiFe-LDH treated by flame for different periods of time.[117] Copyright 2018, Wiley-VCH. (c) Schematic illustration of the synthesis of L-CoOOH *via* LAL and (d) the corresponding magnification of the laser irradiation region. (e) Schematic representation of L-CoOOH with abundant oxygen vacancies for the OER. Color code: white for H, red for O, cyan for Co, and transparent color for a vacancy.[118] Copyright 2019, The Royal Society of Chemistry.

Gui and co-workers used doping and plasma treatment for creating abundant oxygen vacancies into a $LaCoO_3$ perovskite.[103] First, by substituting the lower valence Sr^{2+} ion for La^{3+} ion and then using Ar plasma treatment oxygen vacancies were generated. The prepared $La_{1-x}Sr_xCoO_{3-\delta}$ ($x = 0.3$) sample with doping and Ar plasma treatment showed excellent OER performance and stability, which is attributed to the presence of a large number of oxygen vacancies with high intrinsic activity of active sites. Similarly, the oxygen vacancy rich CoN[104] (N_2 plasma treatment), NiCo-LDH[105] (Ar plasma treatment), NiFe-LDH/ATO[106] (air plasma treatment), $PrBa_{0.5}Sr_{0.5}Co_{1.5}Fe_{0.5}O_{5+\delta}$ (PBSCF)[107] (Ar and H_2 plasma treatment), NiO[108] (Ar plasma treatment), and $CoSe_2$ (Ar/O_2 plasma treatment)[109] electrocatalysts were successfully prepared.

3.2.4. Others. Other methods of forming nanostructured surfaces with oxygen vacancies were found to play a vital role in enhancing electrochemical performance, given that they improved the number of active sites around the defects.[110] Yin and co-workers used the ligand-assisted polyol reduction method to generate oxygen vacancies on cobalt oxide nanoplates.[111] This method converts $Co(OH)_2$ hexagonal nanoplates to CoO_x by heat treatment in the presence of diethylene glycol. The advantage of this method is that it enables large-scale catalyst preparation with superior uniformity, solution dispersion, and controllable concentration of oxygen vacancies on the surface. As shown in Fig. 9a and b, the hexagonal platelet structure of CoO_x was well maintained during the chemical transformation while the interior of the nanoplates became more porous compared to $Co(OH)_2$. This transformation was claimed to be due to the volume shrinkage caused by the phase transition and dehydration of $Co(OH)_2$. The XPS analysis revealed a surface concentration as high as 31% for the oxygen vacancies in CoO_x (Fig. 9c and d). This improves the electrocatalytic performance of oxygen-rich CoO_x for OER.

Ionic liquid-derived electrocatalysts can provide greater active site density and heteroatoms to alter their electronic structures, because of their structural tunability.[112,113] They also have high thermal stability, tunable solvent properties, and good ionic conductivity. Inspired by this, Wang and co-workers generated oxygen vacancies into amorphous N, P and F tri-doped $CoFe_2O_4$ using an ionic liquid as a dopant.[114] They revealed that the ionic liquid played an important role in the formation of the amorphous structure and oxygen vacancies in the catalyst, which are mainly responsible for enhancing the OER performance. Besides the generation of oxygen vacancies, ionic liquids, as mentioned earlier, can facilitate doping of

metal atoms and heteroatoms. Kumbhar and co-workers have developed a simple method to prepare Co and heteroatom (S and N) co-doped carbon (Co_{10}-NS-C) based OER electrocatalysts using ionic liquids.[115] The doping of Co and N/S in carbon modulates the electronic structure of the material, facilitates the electron transfer in the superstructure, and enhances the OER performance with additional stability.

The flame treatment method was introduced as a simple, fast, and green way to generate more precise oxygen vacancies in a safe and open atmosphere.[116,117] Zhou *et al.* used fast flame exposure in ambient conditions to create oxygen vacancies in NiFe-LDH nanosheet arrays.[117] The inner core of a burner flame (4 to 5 cm away from flame gun muzzle) is oxygen-deficient, providing a reducing and yet high-temperature environment to generate oxygen vacancies in NiFe-LDH (Fig. 10a and b). After treatment for 30 s by reducing flame in the open environment, the engraved NiFe-LDH array shows improvement in OER performance.

Like the flame treatment method, laser ablation in liquid (LAL) is also a green, mild and effective approach to introduce oxygen vacancies into transition-metal oxide materials.[118] Zhou and co-workers use LAL to prepare oxygen-rich CoOOH nanosheets by irradiating the Co target immersed in the KOH solution using a nanosecond laser for 20 min (Fig. 10c–e).[118] The oxygen vacancy-rich CoOOH can optimize the adsorption of OER intermediates and improve electrical conductivity, thus enhancing OER performance. Furthermore, Co_3O_4 and $SmMn_2O_5$ with oxygen vacancies have been prepared using laser irradiation to exhibit excellent OER performance.[119,120]

3.3. Alloying

Alloying is considered an efficient strategy to optimize and improve the electrochemical performance of electrocatalysts because by adjusting the elemental composition the electronic structure of the catalysts can be modulated. It is profoundly different than doping methods because of the near stoichiometric presence of the secondary metals. The controlled synthesis of nanocrystal alloys has been demonstrated as an effective approach in various electrochemical reactions, such as OER, hydrogen evolution reaction, nitrogen reduction, and CO_2 reduction, to enhance electrocatalytic activity.[121–124] The basic principle of alloying the electrode's primary metal with others is

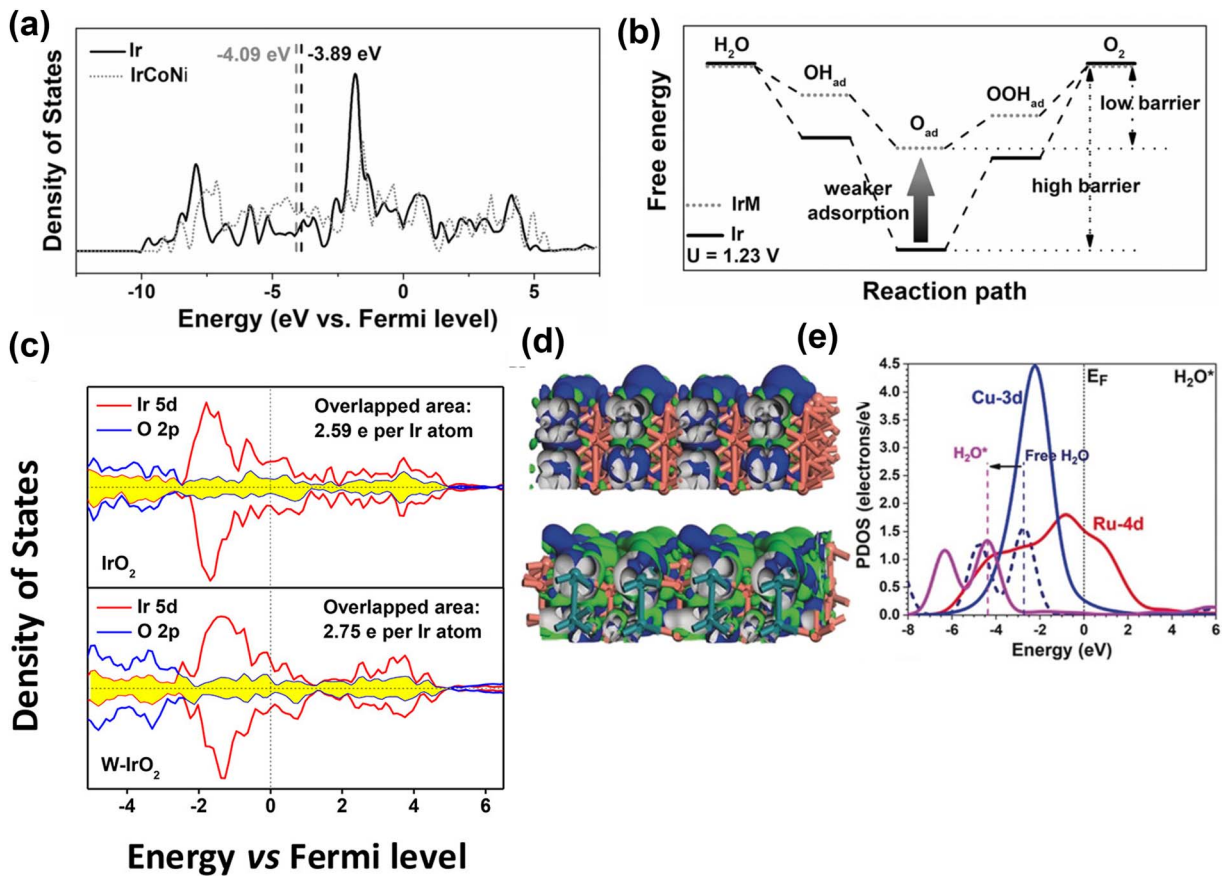

Fig. 11 Computational studies of metal alloy electrocatalysts for OER. (a) Projected DOS of d bands of Ir (black) and IrCoNi models (red) with corresponding d-band center denoted by dash lines. (b) Schematic illustration of reaction paths for OER, indicating alloying Ir with M leads to weaker adsorption of oxygen-based intermediates, thus decreasing the barrier of reaction path.[127] Copyright 2017, Wiley-VCH. (c) Projected density of states of IrO_2 (up) and W-IrO_2 (bottom) with the overlapped states of Ir 5d (red) and O 2p (blue) denoted by the shaded area (yellow).[129] Copyright 2018, American Chemical Society. (d) The side views of the real-spatial contour plots for the bonding and anti-bonding orbitals near the E_F of the pristine RuCu NPs (upper) and channel-rich RuCu NSs (lower). (e) The PDOS of H_2O adsorption on RuCu NSs.[132] Copyright 2019, Wiley-VCH.

to alter the electronic structure of the surface and near-surface atoms of catalyst to enhance the electrochemical activity. For example, the electrocatalytic activity is enhanced by alloying Ir with transition metals because the oxygen adsorption energy can be tuned, as explained by the d-band center theory.[125,126] The d-band center theory describes the relationship between adsorption energy and d-band electrons. Guo and co-workers have prepared IrM (M = Co, Ni, CoNi) porous nanocrystals.[127] The IrM nanocrystal electrocatalysts showed efficient electrocatalytic activity for OER. Their study revealed that Ir induces a ligand effect with transition metals, wherein the d-band center of Ir can be shifted far away from its original Fermi level through alloying. Thus, the adsorption energy of oxygen intermediates decreases, which is the key to improving the electrochemical OER performance (Fig. 11a and b). The same group prepared IrM (M = Ni, Co, Fe) bimetallic nanoclusters *via* a wet-chemical strategy without using surfactants.[128] The *in situ* synthesis without the use of a capping agent (PVP), a cleaner surface, and the strong interaction between IrM nanoclusters enhanced the electrocatalytic performance. Guo and co-workers[129] demonstrated that IrW nano-dendritic structure weakened the adsorption of oxygen intermediates. The projected density of states (Fig. 11c) showed that the overlap between the Ir 5d orbitals and O 2p orbitals of W-IrO_2 (2.75 e^- per Ir atom) is larger than that for IrO_2 (2.59 e^- per Ir atom), suggesting strong interaction between Ir and O in ternary oxide, which enhances the dissolution resistance of Ir and stabilizes the catalytic surfaces. Chen *et al.*[130] synthesized ultrafine Ir_xNi_y alloy using a wet-chemical method, followed by encapsulation in porous N-doped carbon (BMNC) (labeled as Ir_3Ni_2/BMC)

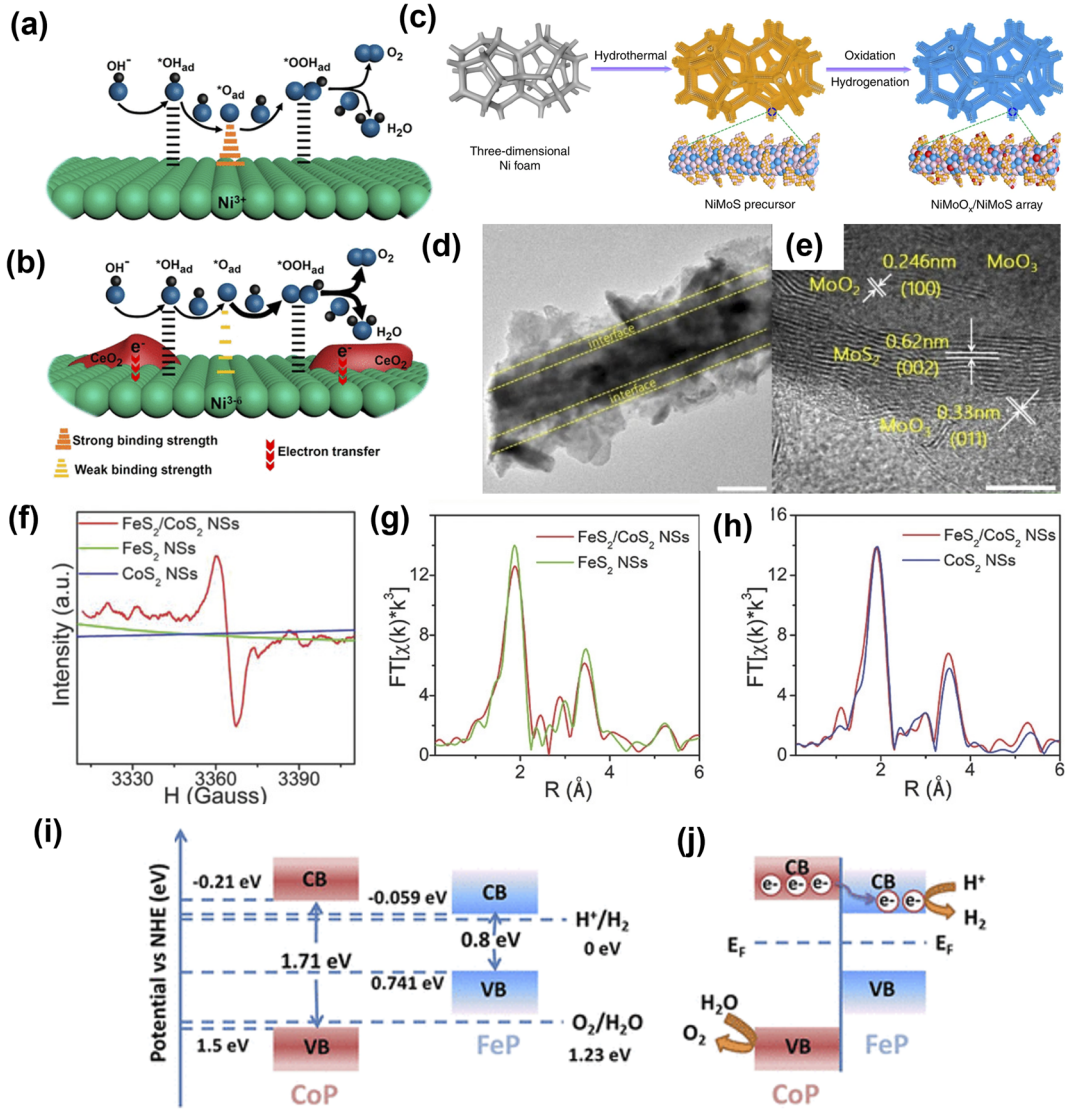

Fig. 12 Heterostructure engineering strategies for OER. (a) Ni@CP and (b) Ni_4Ce_1@CP with the Ni(OH)$_2$–CeO_2 interfaces.[143] Copyright 2018, American Chemical Society. (c) Illustration of transition bimetal oxides/sulfides heterostructure array synthesis. (d and e) HRTEM images of $NiMoO_x$/NiMoS.[144] Copyright 2020, Springer Nature. (f) EPR spectra of FeS_2/CoS_2 NSs, FeS_2 NSs, and CoS_2 NSs. (g) FeS_2/CoS_2 NSs and FeS_2 NSs in *R*-space at the Fe K-edge and (h) FeS_2/CoS_2 NSs and CoS_2 NSs in *R*-space at the Co K-edge. Copyright 2018, Wiley-VCH. (i) Schematic illustrations of the band structure of FeP and CoP before contact. (j) Charge transfer at the interface between CoP and FeP in the CoP-FeP heterostructures.[146] Copyright 2019, American Chemical Society.

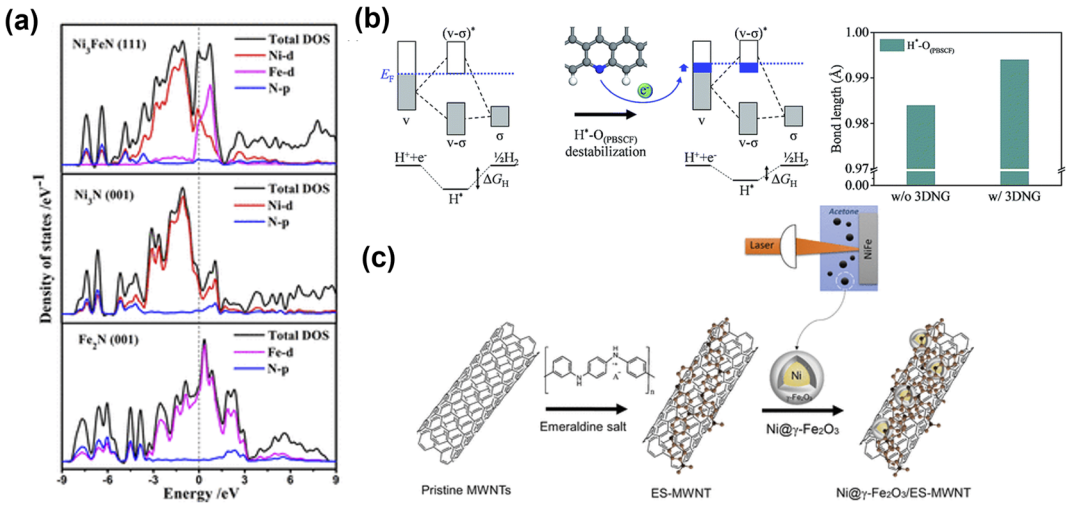

Fig. 13 Metal and carbonaceous materials interface for OER electrocatalysts. (a) Total and partial electronic density of states (TDOS and PDOS) calculated for Ni_3FeN (111), Ni_3N (001), and Fe_2N (001).[149] Copyright 2018. American Chemical Society. (b) Bonding scheme of H*–$O_{(PBSCF)}$ and corresponding ΔG_H (left), and the bond length of H*–$O_{(PBSCF)}$ without and with 3DNG (right).[150] Copyright 2019. The Royal Society of Chemistry. (c) Schematic illustration for the synthesis of the Ni@γ-Fe_2O_3 NPs and the Ni@γ-Fe_2O_3/ES-MWNT hybrid materials.[153] Copyright 2018. American Chemical Society.

derived from bimetallic zeolitic imidazolate frameworks (ZIFs). Owing to the alloying effect between Ni and Ir, increased surface area, and the generation of relatively more active sites, the Ir_3Ni_2/BMC exhibited excellent OER performance with a lower overpotential of 279 mV to deliver 10 mA cm^{-2}. Zhang *et al.*[131] reported Ir (4.9 wt%) incorporation into metallic Ni, significantly improving the electrochemical performance. The theoretical study indicated that the *in situ* generated amorphous Ir–Ni hydroxides around Ni–Ir core were the active species for the OER process, which enhanced the reaction kinetics for OER.

Huang and co-workers[132] prepared channel-rich RuCu snowflake-like nanosheets composed of crystalline Ru and amorphous Cu. The excellent performance of RuCu nanosheets was attributed to highly active electron transfer and optimized electronic structures. The amorphous Cu and localization of bonding and anti-bonding orbitals near Fermi level (E_F) change from Ru sites towards even distribution of the whole surface, supporting the electronic activation near the channel region (Fig. 11d). As shown in Fig. 11e, notable downshifting of H 1s and H_2O 2p bands suggests stronger adsorption to guide the OER process. Feng and colleagues[133] reported that graphitic

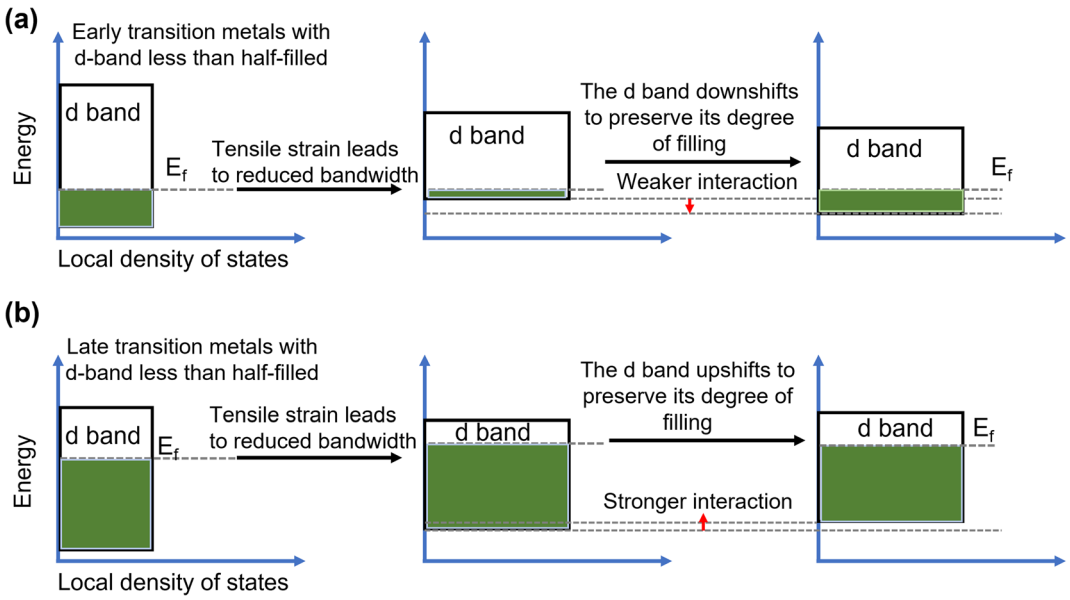

Fig. 14 Mechanism of strain enhanced OER. Energy diagrams showing the influence of (a) tensile and (b) compressive strain on the d band of early transition metals.[163] Copyright 2019. Springer Nature.

carbon encapsulated Ni_xRu_y alloys ($Ni_{0.6}Ru_{0.4}$@C) exhibited excellent performance for OER in 1 M KOH. The experimental and DFT calculation results revealed that minor Ru alloying enabled morphological changes and electronic modulation of the electrocatalysts.

Although Ir and Ru-based electrocatalysts show better electrocatalytic activity in OER, non-precious metal alloy-based electrocatalysts are also noteworthy for use as OER catalysts. Hoang and Gerwirth[134] prepared a NiFe film using an electrodeposition method. The prepared NiFe film showed enhanced OER performance with a lower overpotential of 300 mV at 100 mA cm^{-2} with excellent stability for 72 h. The improved performance of the NiFe film compared to pristine Ni indicates the alteration of electronic structure, which could be due to the interaction between Fe and Ni. Yin and co-workers[135] prepared bimetallic IrNi alloy nanoparticles supported on nickel foam

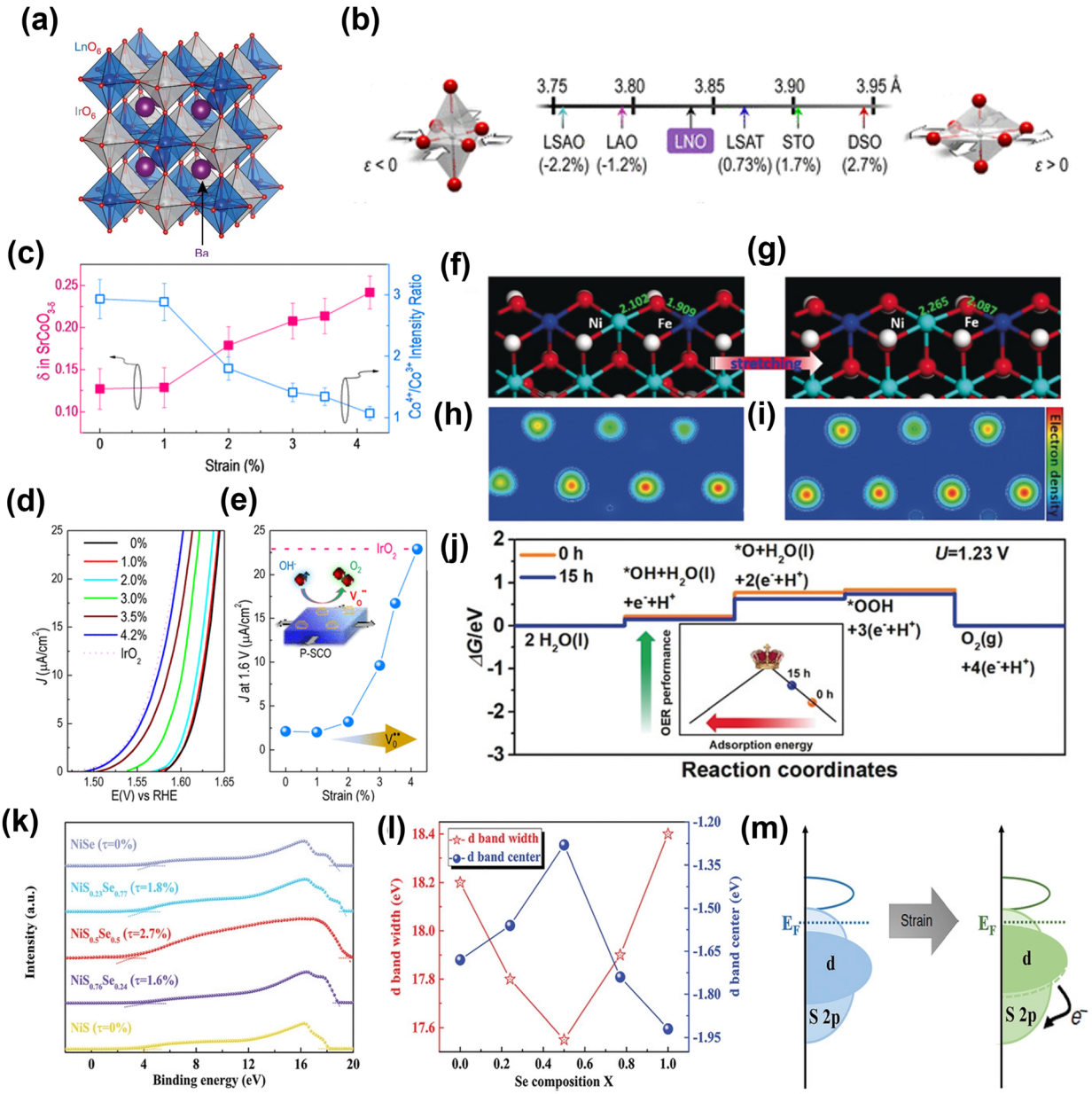

Fig. 15 Performance and computational studies of strain engineered OER electrocatalysts. (a) Crystal structure of a generic Ba_2MIrO_6 DP.[34] Copyright 2016. Springer Nature. (b) Lattice parameters and associated biaxial strain for LNO on various substrates.[162] Copyright 2016. American Chemical Society. (c) Plot of the ratio of the intensities of the Co^{4+} and Co^{3+} peaks showing a clear trend toward decreasing Co valency with tensile strain, with a matching trend in oxygen non-stoichiometry (δ). A strain-relaxed P-SCO film on LSAO ($\varepsilon = 0\%$) was used. (d) Polarization curves for the OER reaction on P-SCO under increasing amounts of biaxial tensile strain. (e) Current densities at 1.6 V *vs.* RHE for all of the films are plotted as a function of strain. The activity for a textured (111) IrO_2 film is included. Theoretical calculations of OER catalysis on NiFe-LDH with and without ball-milling treatment.[167] Copyright 2016. American Chemical Society. (f and g) Slab model. (h and i) Electron density distribution. (j) Free energy profile.[168] Copyright 2019. Wiley-VCH. (k) UPS of samples. (l) The d-band center and corresponding d-bandwidth of the NiS_xSe_{1-x} surface. (m) Schematic of the electron exchange for the lattice-strained surface.[169] Copyright 2020. Wiley-VCH.

substrate using a hydrothermal method. The bimetallic IrNi nanoparticles exhibit excellent catalytic performance with a low overpotential of 200 mV at 20 mA cm^{-2} current density. Wang and colleagues prepared NiFe alloy nanoparticles encapsulated with N-doped carbon with hexagonal close-packed (hcp-NiFe@NC) and face-centered cubic (fcc-NiFe@NC) crystal structures.[136] The hcp-NiFe@NC catalyst exhibits superior OER performance with 226 mV overpotential at 10 mA cm^{-2}, which is much lower than fcc-NiFe@NC (292 mV @ 10 mA cm^{-2}). The excellent performance of hcp-NiFe@NC was claimed to be due to the hcp structure (space group: $P6_3/mmc$) and favorable electronic properties to expedite the reaction on N-doped carbon. Liu *et al.* prepared a Fe–Co–P alloy sphere using Fe–Co metal–organic complex (MOC) as a precursor.[137] The results suggested that the electrochemically induced high-valent Fe stabilized Co in a low valence state, which enabled the enhancement of OER performance and stability of the Fe–Co–P alloy. Wang and Co-workers fabricated nickel-iron diselenide hollow nano-chains (NFSHNCs) as an OER catalyst.[138] They found that O* and OH* adsorption was found to be closely related to the iron and nickel sites. This strategy was used by several researchers to prepare metal alloys and study them extensively as OER electrocatalysts such as Ni–Mo alloy microspheres,[139] Mo–Ni alloy nanoparticles,[140] Ru–Ni nanosheets,[141] and monolithic nanoporous Ni–Fe alloys.[142]

3.4. Heterostructure engineering

Heterostructures are conjoined electrocatalytic domains of independent nature and generally constructed by integrating different components such as metal–metal interfaces, metal–oxide interfaces, metal–non oxide (sulfide, nitride, selenide, and carbide) interfaces, and other interfaces (oxide–chalcogenide, oxide–oxide, phosphate-tungstate). Such interface engineering plays an essential role in improving the OER performance, which is due to: (a) modulating the electronic structure and therefore optimizing reaction intermediates, and (b) providing abundant catalytically active sites for electrolysis. It also helps to change the intrinsic catalytic activities of individual components, enabling catalysts with unique physicochemical properties towards electrochemical reactions. The electronic interactions among the different components create new active centers through the interface effect, enhancing the electrocatalytic performance. In short, interface engineering alters the electronic structure of an electrocatalyst, which could make it favorable for OER efficiency.

Huang and co-workers constructed a $Ni(OH)_2$–CeO_2 heterostructure supported on carbon paper (Ni_xCe_y@CP).[143] The interface induced by the strong electronic interaction between hydroxide ($Ni(OH)_2$) and oxide (CeO_2) favorably modulated the binding strength between reaction intermediates and the electrocatalyst, which enhanced the OER performance (Fig. 12a and b). Zhai *et al.* fabricated a transition metal-based hierarchical bimetal oxide/sulfide heterostructure array ($NiMoO_x$/NiMoS) by an oxidation/hydrogenation-induced surface reconfiguration strategy (Fig. 12c–e).[144] The as-prepared $NiMoO_x$/NiMoS heterostructure arrays exhibited excellent electrocatalytic performance for OER with 186, 225, 278, and 334 mV to reach 10, 100, 500, and 1000 mA cm^{-2}, respectively. The excellent performance of transition bimetal oxides/sulfides heterostructure arrays was attributed to simultaneous modulation of component and geometric structures, and systematic optimization of charge transfer, increased active sites, and synergy between heterostructure interfaces. Jiang and co-workers[145] designed metal alloys (Co_3Mo) and metal oxide ($CoMoO_x$) heterostructures ($Co_3Mo/CoMoO_x$) by a facile topological transformation through direct annealing of $CoMoO_4$ under H_2 atmosphere. The $Co_3Mo/CoMoO_x$ heterostructure with abundant and strong coupling interfaces was shown to synergistically strengthen the conductivity of $Co_3Mo/CoMoO_x$ and accelerate the charge transfer kinetics.

Li *et al.*[146] prepared defect-rich FeS_2/CoS_2 interface nanosheets. The synthesized FeS_2/CoS_2 showed remarkable OER activity with an overpotential of 302 mV at 100 mA cm^{-2}, benefiting from the abundant defects present in the nanosheets interface structure. As shown in Fig. 12f, the electron paramagnetic resonance (EPR) spectra of FeS_2/CoS_2 with stronger EPR signal suggested abundant S vacancies compared to FeS_2 and CoS_2. Also, peak intensities of Fe–S and Fe–Fe pairs in the extended X-ray absorption fine structure (EXAFS) spectrum of FeS_2/CoS_2 were lower than FeS_2, further indicating disordered and defective interfaces (Fig. 12g and h). Feng *et al.* demonstrated that a MoS_2/Ni_3S_2 heterostructure exhibited excellent OER performance due to a precise interface that was synergistically favoring the chemisorption of oxygen-containing intermediates[147] on the catalyst surface. Ai and co-workers[148] showed non-precious metal phosphide heterostructures (CoP-FeP) as efficient electrocatalysts. A hierarchical branched CoP-FeP heterostructure is directly grown on a carbon cloth (CC). The n-type CoP semiconductor had a bandgap of 1.71 eV and conduction band position at −0.21 eV *vs.* normal hydrogen electrode (NHE), while FeP featured a bandgap of 0.8 eV with a conduction band position of −0.059 (Fig. 12i and j). The CoP displayed a lower work function than that of the FeP and due to intimate contact between CoP and FeP, the electrons flowed from CoP to FeP. This was mainly because of the built-in electric field at the interface until the work function equilibrium is reached. The optimized electron density and electronic potential distribution at the surfaces was thought to promote charge transfer to adsorbates and strengthen the chemical adsorption, thus enhancing electrocatalytic activity.

Another common strategy to improve electrochemical performance and stability is hybridizing electrocatalysts with carbonaceous materials. Yu *et al.*[149] prepared Ni_3FeN nanoparticles on reduced graphene oxide (Ni_3FeN/r-GO) as efficient electrocatalysts. The excellent performance of Ni_3FeN/r-GO heterostructures was attributed to abundant active sites and high electrical conductivity of bimetallic nitrides, and efficient mass transport of the r-GO framework. The DOS calculations (Fig. 13a) indicated that the band structure of Ni_3FeN was consecutive near the Fermi level, suggesting Ni_3FeN was intrinsically metallic, suggesting a strong covalent interaction between Ni, Fe, and N. The Ni_3N and Fe_3N have only one metal track to contribute DOS value, which indicates that at the

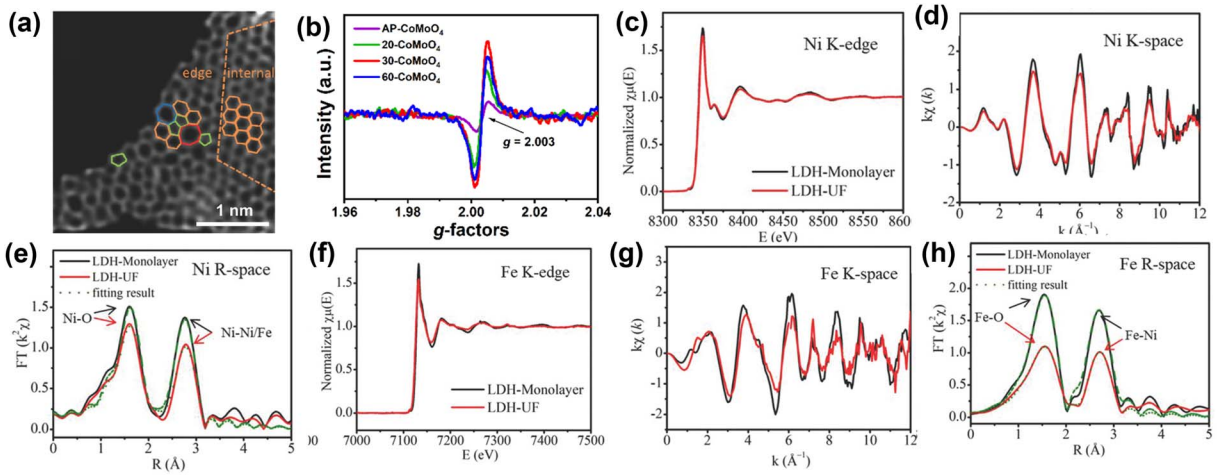

Fig. 16 Characterizations employed for the elucidation of structural imperfections and resultant alterations of the electronic structure (a) HAADF image of DG with an acceleration voltage of 80 kV. Hexagons, pentagons, heptagons, and octagons were labeled in orange, green, blue, and red, respectively.[173] Copyright 2016. Wiley-VCH (b) EPR of AP-$CoMoO_4$ and *n*-$CoMoO_4$.[176] Copyright 2022. Wiley-VCH (c) (*A*) Ni K-edge XANES spectra, (d) Ni K-edge EXAFS oscillation functions $k^2\chi$ (*k*), and (e) magnitude of k^2-weighted FT of the Ni K-edge EXAFS spectra. (f) Fe K-edge XANES spectra, (g) Fe K-edge EXAFS oscillation functions $k^2\chi$ (*k*), and (h) magnitude of k^2-weighted FT of the Fe K-edge EXAFS spectra for LDH-Monolayer and LDH-UF, respectively.[178] Copyright 2018. Wiley-VCH.

Ni_3FeN and r-GO interface, the number of electrons transferred from Ni_3FeN to the r-GO layer was increased, which then regulated the charge redistribution at the interface between Ni_3FeN and r-GO. Such electron transfer causes the hole accumulation on Ni_3FeN, which promotes OER intermediate reaction with optimal binding energy values. The Ni_3FeN exhibited excellent performance with low overpotential of 270 mV at 10 mA cm^{-2}. Kim and co-workers prepared a composite electrocatalyst (P-3G) containing cation-ordered perovskite ($PrBA_{0.5}Sr_{0.5})_{0.95}Co_{1.5}Fe_{0.5}O_{5+\delta}$ (PBSCF) and 3D porous N-doped graphene (3DNG).[150] The DFT calculations revealed that the energy gap decreased because ε_d came close to the Fermi level (E_F). The reduced energy gap describes the relatively strong hybridization between the transition metal and lattice oxygen. The increased covalency between transition metals and lattice oxygen in PBSCF was triggered by the electron transfer of 3DNG, which boosted the OER performance (Fig. 13b). Also, for OER, the active sites were located at the surface of PBSCF and were mainly responsible for high OER performance. Tahir *et al.*[151] prepared hybrid Co_3O_4 embedded in tubular nanostructures of graphitic carbon nitride (GCN). The strong synergy between Co_3O_4 and GCN played an essential role in enhancing OER performance. The high surface area, unique tubular structure, and composition of hybrid electrocatalysts made almost all redox sites readily available for catalysis and provided faster ionic and electronic conduction. Liu's group prepared $NiCo_2P$ nanosheets on functionalized carbon nanotubes ($NiCo_2P_x$/CNTs) as cost-efficient, highly active electrocatalysts.[152] During the OER, the $NiCo_2P_x$ was converted into NiCo-LDH, which acted as the active catalyst, while CNT remained as conductive support and improved the stability of the hybrid electrocatalyst. To boost the electrochemical performance of a Ni@γ-Fe_2O_3 core–shell, multiwalled carbon nanotube functionalized with nitrogen-rich emeraldine salt (ES-MWNT) was used as the catalyst support (Fig. 13c).[153] The N enriched MWNT enhanced the interaction with the γ-Fe_2O_3 shell, which modified the catalyst surface and created a highly durable catalyst. In addition to the above-mentioned heterostructures, other hybrid electrocatalysts with carbonaceous materials have been developed such as $Fe_1Co_3O_x$@C-800,[154] MnO_2/G/CNT,[155] CoP/VGNHs,[156] Co_3O_4/CNTs,[157] and Co_9S_8/N,S-rGO[158] with a unique heterostructure and good electrocatalytic OER activity.

In heterostructured electrocatalysts, the interface effect can efficiently optimize the electron transfer and enhance the electrochemical performance by (a) lowering the interfacial resistance and adsorption energy of oxygen, (b) improving the electron-withdrawing ability and creating the metal–oxygen interface, and (c) boosting synergy between compositions through unique reaction steps.

3.5. Strain engineering

In recent years, strain engineering for nanostructures has gained attention in electrochemical reactions including OER, HER, alcohol oxidation reactions, CO_2 reduction, and N_2 reduction reactions. Strain is the deformation of a solid caused by stress and is a dimensionless quantity. Experimental and theoretical studies have suggested that creating strain in materials can successfully modulate the electronic structure.[159] Thus, introducing strain is a viable technique for altering the electronic structure and boosting the electrocatalytic activity of nanomaterials. Since electronic structure modulation is closely tied to the d-band center of a material and thus the performance in electrocatalytic processes like OER, numerous reports exist with regard to how the d-band center position relative to the Fermi level is altered under applied strain, as shown in Fig. 14a and b.[160] When tensile or compressive strain is applied to transition metals (more than half-filled d-band), the d-orbital

Table 1 Representative research progress of OER electrocatalysts with modulated electronic structures

Electrocatalyst	Strategy	Overpotential (mV) at 10 mA cm^{-2}	Reference
Mo-$NiCo_2O_4$/$Co_{5.47}N$/NF	Doping	370	184
Ru-RuP_x-Co_xP	Doping	291	185
Ni_3P:FeMo	Doping	250	23
NiVIr-LDH	Doping	180	186
N-CoFe LDHs	Doping	281	65
Co/Ce-Ni_3S_2/NF	Doping	286 @ 20 mA cm^{-2}	77
Ru/Ni-Co_3O_4	Doping	290	78
Co, Nb-MoS_2/TiO_2 HSs	Doping	260	80
Defect-rich Co_3O_4 nanosheets	Oxygen vacancy	200	89
Fe_1Co_1-ONS	Oxygen vacancy	308	92
$PrBaCo_2O_{5.75}$	Oxygen vacancy	360	95
CoFe LDHs nanosheets	Oxygen vacancy	232	98
NiFe-LDH	Oxygen vacancy	310	99
Co_3O_{4-x}	Oxygen vacancy	330	100
Plasma-engraved Co_3O_4 nanosheets	Oxygen vacancy	300	85
Vo-$MnCo_2O_4$	Oxygen vacancy	400	102
$La_{1-x}CoO_{3-\delta}$ ($x = 0.3$)	Oxygen vacancy	326	103
NiFe-LDH	Oxygen vacancy	250	117
Co_3O_4	Oxygen vacancy	298	119
Ir_3Ni_2/BMNC	Alloying	279	130
$Ni_{0.93}Ir_{0.07}$/rGO	Alloying	271.8	131
RuCu NSs/C-350 °C	Alloying	234	132
e-$Ni_{0.6}Ru_{0.4}$@C	Alloying	278 @ 100 mA cm^{-2}	133
FeIr/NF	Alloying	200 @ 20 mA cm^{-2}	135
$Fe_{60}(CoNi)_{30}Cr_{10}$	Alloying	187	187
NiCoFeMoMn high-entropy alloy	Alloying	350 @ 1000 mA cm^{-2}	188
$NiMoO_x$/NiMoS	Heterostructure	186	144
Co_3Mo/$CoMoO_x$	Heterostructure	256	145
$CoSe_2$@$MoSe_2$	Heterostructure	309	189
Co_3O_4@Mo-Co_3S_4-Ni_3S_2/NF	Heterostructure	295 @ 50 mA cm^{-2}	190
CoP-FeP	Heterostructure	250	148
Co@CoP_2/CF	Heterostructure	210	191
WO_2-$Ni_{17}W_3$/$NiFe(OH)_x$	Heterostructure	240 @ 50 mA cm^{-2}	192
NiSe@CoFe LDH	Heterostructure	203	193
$NiCo_2P_x$/CNTs	Heterostructure	284	152
CoFe-OH@FeOOH	Heterostructure	200	194
NiFe-LDH	Strain engineering	270	168
NiS_xSe_{1-x} NNH	Strain engineering	257	169
$Na_{0.7}CoO_2$-Ag	Strain engineering	236	195
Ni_3Al alloy	Strain engineering	280	196
Co@N_1-GY	Strain engineering	330	197
Co_2P/Ni_2P-2% Mo	Strain engineering	319 @ 50 mA cm^{-2}	198
Ni_3FeN/Ni_3Fe	Strain engineering	250	199
Ru-$ZnIn_2S_4$	Strain engineering	276 @ 50 mA cm^{-2}	200
NiFe-MOF	Strain engineering	300 mV	201

overlap changes accordingly, giving rise to a sharpening of the d-band and a shift in its d-band center to preserve the degree of d-band filling. As the electrochemical performance of a material directly correlates to its electronic structure, it can, therefore, be effectively tuned by strain engineering. Various methods have been used to generate strain in the catalysts including epitaxial growth of thin films,[161,162] formation of bimetallic nanoparticles[163] and crystal morphology engineering.[164]

Through first-principles calculations, Yildiz and coworkers[165] showed a planar strain effect on the oxygen-vacancy formation and oxygen adsorption in $LaCo_3$. The adsorption of oxygen molecules transitioned from chemisorption to physisorption at high strain. Adjusting with charge-density profiles, the density of electronic states, and stress threshold, they proposed the possibility of tuning strain-mediated reactivity in $LaCo_3$ and other related perovskites. Later, several studies explored the effect of strain on surface reactivity. Koper and coworkers[34] developed electrocatalysts based on iridium double perovskites (Ir DPs), which contain 32 wt% less iridium than IrO_2 and yet exhibit more than threefold higher activity in acid electrolyte. Double perovskites (DPs) have a general formula of $A_2BB'O_6$, where A denotes a large cation and B and B′ smaller cations. Fig. 15a shows the crystal structure of an ideal DP. The high catalytic activity of Ir DPs is thought to be due to the crystal lattice strain caused by the small Lanthanide and Yttrium cations in the B′ site of the DPs. As IrO_2 and oxygen bind strongly, the lattice strain caused by the substitution of smaller lanthanides or yttrium weakens the oxygen adsorption energy

and therefore improves the activity of the Ir DPs in comparison to IrO_2.

In another example, an n-doped rutile TiO_2 film is directly grown on NiTi foil, and its catalytic performance was examined after applying tensile strain.[166] The tensile strain increased the density of surface accessible sites and lowered the activation barrier in the reaction pathway. Stoerzinger *et al.*[161] demonstrated that epitaxial strain *via* lattice mismatch could tune the activity of oxygen electrocatalysis of $LaCoO_3$ in alkaline solutions. The moderate tensile strain can further induce changes in the electronic structure leading to an enhanced electrocatalytic performance by $LaCoO_3$. Lee and co-workers[162] systematically determined the effect of epitaxial strain on the conducting perovskite $LaNiO_3$. They used epitaxially strained $LaNiO_3$ ranging from tensile (+) to compressive (−) to check its influence on OER over a range of lattice-mismatched substrates, which included (001) $LaSrAlO_4$ (LSAO), (001) $LaAlO_3$ (LAO), (001) $(LaAlO_3)_{0.3}(SrAl_{0.5}Ta_{0.5}O_3)_{0.7}$ (LSAT), (001) $SrTiO_3$ (STO), and (001)pc $DyScO_3$ (DSO) (Fig. 15b). The results suggest that moderate tensile strain can induce change in electronic structure, leading to enhanced electrochemical OER performance. The same group also used a perovskite-based strontium cobaltite (P-SCO) thin film to show that epitaxial strain could tune the oxygen stoichiometry under conditions consistent with the OER.[167] The epitaxial strain regulates the oxygen vacancies and Co^{4+}/Co^{3+} ratio in P-SCO film (Fig. 15c). The P-SCO film with 4.2% strain matches electrocatalytic activity with noble-metal IrO_2 catalyst (Fig. 15d and e).

Liu and co-workers[168] used a facile ball-milling method to improve the binding strength of NiFe-LDH to oxygenated intermediates *via* generated tensile strain, which reduced the anti-bonding filling states in the d orbitals and thus facilitated the adsorption of oxygenated intermediates. DFT calculations gave further insight into the relation between lattice strain and OER kinetics. Fig. 15f and g shows the stretched Ni–O and Fe–O (stretched by 0.16 Å) to simulate the ball-milled NiFe-LDH. Fig. 15h and i compare the electron densities around the Ni and Fe sites in NiFe-LDH, which clearly show the electron-rich structure of NiFe-LDH with tensile strain. The calculated OER (Fig. 15j) overpotential decreases from 0.55 to 0.48 eV and Gibbs free energy for every elementary step is optimized after introducing tensile strain in NiFe-LDH. This is believed to be due to the enhanced adsorption for oxygenated intermediates, which moves NiFe-LDH towards the vertex of the activity volcano (inset in Fig. 15j).

Deng and co-workers[169] prepared NiS_xSe_{1-x} nanorods@nanosheets hybrids (NiS_xSe_{1-x} NNH) on Ni foam (NF) and induced the strain-effect both on the surface and in the interior of the materials. The results showed dramatic improvement in electrochemical performance. It was suggested that $NiS_{0.5}Se_{0.5}$ electrocatalyst with $\approx$2.7% lattice strain exhibits the best oxygen evolution reaction (OER) performance with low overpotentials of 257 mV at 10 mA cm^{-2}, with long-term stability for 300 h at 10 and even 100 mA cm^{-2}. The $NiS_{0.5}Se_{0.5}$ has a lower work function and high Fermi level compared to other samples, as shown in Fig. 15k, which verify that the $NiS_{0.5}Se_{0.5}$ possesses the highest electrical conductivity. Also, with an increase in lattice strain, the d-band width decreases, with the d-band of the composite shifting closer to the Fermi level (Fig. 15l). Evidently the generated strain narrowed the bandwidth and thus influences the electronic structure of the material. With an upshift of the d-band center, the adsorption interaction with the reaction intermediates is improved, thus fostering enhanced activity (Fig. 15m).

Recently, Yan and coworkers[170] proposed a facile strategy to introduce lattice strain in the metal–organic framework (MOF). They employed monocarboxylic acid as the linker scission to replace part of binary carboxylic acid in NiFe-MOF. The as-prepared lattice-strained NiFe-MOF exhibited superior OER performance with 230 mV overpotential to reach 10 mA cm^{-2} in alkaline electrolyte. Using the XAS and synchrotron radiation Fourier transform infrared spectroscopy (SR-FTIR) studies, it was observed that during OER the key *OOH intermediate was adsorbed on high-valence $Ni^{3+}/^{4+}$ sites. This suggests $Ni^{3+}/^{4+}$ sites were the most active sites for OER in which the rate-limiting step is the formation of *OOH. First-principles study indicates that the electronic structure of Ni active sites in MOFs can be modulated by lattice strain, enhancing the OER performance of NiFe-MOFs.

4. Characterization of electrocatalysts

Understanding the structure of the electrocatalyst using characterization helps to elucidate the relationship between structure and the physical and electrochemical properties. Herein, we have summarized some quantitative and qualitative characterization techniques. Powder X-ray Diffraction (PXRD) and Electron Microscopy (EM) are the most commonly utilized tools to glean basic information about changes in a material when it undergoes electronic structure modulations. In particular, advanced aberration-corrected transmission electron microscopy (ACTEM) can be used to characterize defects such as oxygen and sulfur vacancies.[171,172] Yao and coworkers[173] used ACTEM analysis to visualize the defect regions of materials (Fig. 16a). XPS can be used to analyze surface chemical states and gather other electronic information. Recently, Gao *et al.* verified oxygen vacancies in NiFe LDH by analyzing the O1s XPS spectrum.[174] Electron paramagnetic resonance (EPR) spectroscopy is commonly used to elucidate oxygen vacancies in nanomaterials.[175] For example, Xiao *et al.*[176] used EPR to prove the existence of oxygen vacancies in electrocatalysts. As shown in Fig. 16b, the EPR signal peak at $g = 2.003$ indicates the electrons have been captured by the defects, confirming the existence of free electrons trapped in oxygen vacancies. With the rapid development of synchrotron radiation sources, X-ray absorption spectroscopy (XAS) techniques including extended X-ray absorption fine structure (EXAFS) and X-ray absorption near edge structure (XANES) analysis have become an invaluable and effective characterization method to check the changes in the electronic structure around the active center.[177] Zhang *et al.*[178] used XANES and EXAFS to explore the defects in ultrafine monolayer NiFe LDH structure (LDH-UF). The EXAFS data

conclusively suggests the existence of multivacancies (oxygen, Ni, and Fe vacancies) in LDH-UF. The presence of these vacancies dramatically alters the LDH electronic structure and electrochemical properties (Fig. 16c–h).

5. Conclusion and outlook

The design and development of an efficient OER electrocatalyst for water splitting carries great significance. This article has outlined the recent research efforts on electronic structure modulation of electrocatalysts, including transition-metal-based nanomaterials, noble metals, and perovskite oxides for the OER. Key strategies for tuning the electronic structure of the electrocatalyst, such as alloying, doping, creating oxygen vacancies, heterostructure engineering, and strain engineering, are introduced, and their effect in enhancing the OER performance are discussed. Through these discussions, it is clear that electronic structure modification is the most effective method for improving electrochemical performance (Table 1). Although significant research progress has been made, many significant challenges continue to exist and require careful design and analysis. Going forward, here are a few, although not exhaustive, suggestions that researchers can keep in mind in the search for more efficient OER catalysts:

(a) While taking into account the most popular strategies that have been documented in this paper, new ground must be explored such as combinatorial versions of established methods. Using a combination of alloying and interface engineering, Liu *et al.*[179] demonstrated an $NiFe(OH)_x$/(Ni,Fe)Se_2/CC catalyst that showed far superior OER performance to typically reported $NiFe(OH)_x$ catalysts, whose OER performance is impeded by poor electrical conductivity. Without further doping, the Xie group demonstrated a dual modulation strategy wherein electrochemical reduction activation generated poorly crystalline CoO islands interfaced with highly crystalline Co_3O_4 nanowires.[180] This led to the generation of the key active component oxygen-vacancy rich CoOOH layer responsible for a 10-fold OER performance enhanced compared to pristine Co_3O_4. Doping metal atoms into alloys to further enhance their OER performance has also been documented and is a domain that should be pursued by prospective researchers. Qiao *et al.*[181] recently reported Fe-doped intermetallic Co_2B, which demonstrated OER activity surpassing that of IrO_2.

(b) During electrochemical measurements, the vacancies, strain, and heterostructure interfaces can change over time. The *ex situ* or conventional characterizations may not reflect the active catalytic centers. Significant advances in *in situ* spectroscopic techniques (*e.g.*, *in situ* Fourier-transform infrared spectroscopy and *in situ* Raman spectroscopy, and *in situ* XAS) as well as time-resolved measurements have shown promise in providing in-depth insight into electrocatalytic behaviour. These *in situ* characterizations could provide real-time information on potential structural changes, chemical states, and reaction mechanisms under varying electrochemical measurement conditions. The results will be helpful to improve the performance and stability of electrocatalysts and binding trends along with parameters for databases. Ongoing efforts to gather data from numerous experiments have since enhanced theoretical calculations too.[182]

(c) The experimental characterizations suggest that the electrocatalysts go through chemical and physical changes during OER. Hence, relying on theoretical models to predict the behavior of an electrocatalytic material is a path that more researchers should consider adopting.[183] Current advances in first principles-based studies can provide insight into morphological or structural changes a material will undergo in various electrochemical environments, even if these studies are not exhaustive. All the electronic structure modulation strategies covered in this review lend themselves to effective scrutiny *via* modern theoretical tools. Researchers can consider using these existing analyses to design their catalytic materials.

In summary, targeted analysis should focus on designing efficient, stable, and scalable electrocatalysts for OER. Such approaches will allow enhancements in the capabilities of new electrocatalysts, through continuous efforts on the electronic structure modulation-based material design. Improved synthetic strategies will enable the development of promising electrocatalysts to usher in a greener energy economy facilitated by efficient water splitting.

Conflicts of interest

There are no conflicts to declare.

Acknowledgements

This work is supported by the King Abdullah University of Science and Technology (KAUST).

References

1 N. S. Lewis, *Science*, 2016, **351**, aad1920.
2 H. Tao, Q. Fan, T. Ma, S. Liu, H. Gysling, J. Texter, F. Guo and Z. Sun, *Prog. Mater. Sci.*, 2020, **111**, 100637.
3 J. A. Turner, *Science*, 2004, **305**, 972–974.
4 I. Roger, M. A. Shipman and M. D. Symes, *Nat. Rev. Chem.*, 2017, **1**, 0003.
5 J. H. Montoya, L. C. Seitz, P. Chakthranont, A. Vojvodic, T. F. Jaramillo and J. K. Nørskov, *Nat. Mater.*, 2017, **16**, 70–81.
6 K. Zhu, F. Shi, X. Zhu and W. Yang, *Nano Energy*, 2020, **73**, 104761.
7 Y.-R. Zheng, J. Vernieres, Z. Wang, K. Zhang, D. Hochfilzer, K. Krempl, T.-W. Liao, F. Presel, T. Altantzis, J. Fatermans, S. B. Scott, N. M. Secher, C. Moon, P. Liu, S. Bals, S. Van Aert, A. Cao, M. Anand, J. K. Nørskov, J. Kibsgaard and I. Chorkendorff, *Nat. Energy*, 2022, **7**, 55–64.
8 M. G. Walter, E. L. Warren, J. R. McKone, S. W. Boettcher, Q. Mi, E. A. Santori and N. S. Lewis, *Chem. Rev.*, 2010, **110**, 6446–6473.
9 D. H. Kweon, M. S. Okyay, S.-J. Kim, J.-P. Jeon, H.-J. Noh, N. Park, J. Mahmood and J.-B. Baek, *Nat. Commun.*, 2020, **11**, 1278.

10 S. Y. Bae, J. Mahmood, I. Y. Jeon and J. B. Baek, *Nanoscale Horiz.*, 2019, **5**, 43–56.
11 A. N. Rollinson, J. Jones, V. Dupont and M. V. Twigg, *Energy Environ. Sci.*, 2011, **4**, 1216.
12 A.-L. Wang, H. Xu and G.-R. Li, *ACS Energy Lett.*, 2016, **1**, 445–453.
13 R. Souleymen, Z. Wang, C. Qiao, M. Naveed and C. Cao, *J. Mater. Chem. A*, 2018, **6**, 7592–7607.
14 S. Z. Oener, L. P. Twight, G. A. Lindquist and S. W. Boettcher, *ACS Energy Lett.*, 2021, **6**, 1–8.
15 X. Zou and Y. Zhang, *Chem. Soc. Rev.*, 2015, **44**, 5148–5180.
16 C. Z. Yuan, K. S. Hui, H. Yin, S. Zhu, J. Zhang, X. L. Wu, X. Hong, W. Zhou, X. Fan, F. Bin, F. Chen and K. N. Hui, *ACS Mater. Lett.*, 2021, **3**, 752–780.
17 S. Rafai, C. Qiao, Z. Wang, C. Cao, T. Mahmood, M. Naveed, W. Younas and S. Khalid, *ChemElectroChem*, 2019, **6**, 5469–5478.
18 S. Anantharaj, S. Kundu and S. Noda, *Nano Energy*, 2021, **80**, 105514.
19 P. Babar, A. Lokhande, H. H. Shin, B. Pawar, M. G. Gang, S. Pawar and J. H. Kim, *Small*, 2018, **14**, 1702568.
20 P. Babar, A. Lokhande, V. Karade, I. J. Lee, D. Lee, S. Pawar and J. H. Kim, *J. Colloid Interface Sci.*, 2019, **557**, 10–17.
21 S. Z. Oener, M. J. Foster and S. W. Boettcher, *Science*, 2020, **369**, 1099–1103.
22 P. Babar, K. Patil, V. Karade, K. Gour, A. Lokhande, S. Pawar and J. H. Kim, *ACS Appl. Mater. Interfaces*, 2021, **13**, 52620–52628.
23 S. M. Pawar, A. T. Aqueel Ahmed, C. H. Lee, P. T. Babar, J. H. Kim, S. U. Lee, H. Kim and H. Im, *ACS Appl. Energy Mater.*, 2021, **4**, 14169–14179.
24 N. Mushtaq, Z. Wang, H. Tabassum, M. Tahir, Z. Han, Y. Zhu, W. Younas, X. Ma and C. Cao, *Dalt. Trans.*, 2022, **51**, 6285–6292.
25 J. S. Kim, B. Kim, H. Kim and K. Kang, *Adv. Energy Mater.*, 2018, **8**, 1702774.
26 P. T. Babar, A. C. Lokhande, M. G. Gang, B. S. Pawar, S. M. Pawar and J. H. Kim, *J. Ind. Eng. Chem.*, 2018, **60**, 493–497.
27 Y. Yan, B. Y. Xia, B. Zhao and X. Wang, *J. Mater. Chem. A*, 2016, **4**, 17587–17603.
28 P. T. Babar, A. C. Lokhande, B. S. Pawar, M. G. Gang, E. Jo, C. Go, M. P. Suryawanshi, S. M. Pawar and J. H. Kim, *Appl. Surf. Sci.*, 2018, **427**, 253–259.
29 H. Boumeriame, E. S. Da Silva, A. S. Cherevan, T. Chafik, J. L. Faria and D. Eder, *J. Energy Chem.*, 2022, **64**, 406–431.
30 K. Patil, P. Babar, D. M. Lee, V. Karade, E. Jo, S. Korade and J. H. Kim, *Sustain. Energy Fuels*, 2020, **4**, 5254–5263.
31 S. Anantharaj, S. R. Ede, K. Sakthikumar, K. Karthick, S. Mishra and S. Kundu, *ACS Catal.*, 2016, **6**, 8069–8097.
32 N. Han, P. Liu, J. Jiang, L. Ai, Z. Shao and S. Liu, *J. Mater. Chem. A*, 2018, **6**, 19912–19933.
33 R. Khan, M. T. Mehran, S. R. Naqvi, A. H. Khoja, K. Mahmood, F. Shahzad and S. Hussain, *Int. J. Energy Res.*, 2020, **44**, 9714–9747.
34 O. Diaz-Morales, S. Raaijman, R. Kortlever, P. J. Kooyman, T. Wezendonk, J. Gascon, W. T. Fu and M. T. M. Koper, *Nat. Commun.*, 2016, **7**, 12363.
35 C. Qiao, Z. Usman, T. Cao, S. Rafai, Z. Wang, Y. Zhu, C. Cao and J. Zhang, *Chem. Eng. J.*, 2021, **426**, 130873.
36 C. Qiao, S. Rafai, T. Cao, Z. Wang, H. Wang, Y. Zhu, X. Ma, P. Xu and C. Cao, *ChemCatChem*, 2020, **12**, 2823–2832.
37 L. Li, P. Wang, Q. Shao and X. Huang, *Chem. Soc. Rev.*, 2020, **49**, 3072–3106.
38 J. He, Y. Zou and S. Wang, *Dalt. Trans.*, 2018, **48**, 15–20.
39 N. Mushtaq, C. Qiao, H. Tabassum, M. Naveed, M. Tahir, Y. Zhu, M. Naeem, W. Younas and C. Cao, *Sustain. Energy Fuels*, 2020, **4**, 5294–5300.
40 D. Zhou, P. Li, X. Lin, A. McKinley, Y. Kuang, W. Liu, W. F. Lin, X. Sun and X. Duan, *Chem. Soc. Rev.*, 2021, **50**, 8790–8817.
41 Z.-P. Wu, F. Lu, S.-Q. Zang, X. Wen, D. Lou, Z.-P. Wu, X. F. Lu, X. W. Lou and S.-Q. Zang, *Adv. Funct. Mater.*, 2020, **30**, 1910274.
42 Q. Pan and L. Wang, *J. Power Sources*, 2021, **485**, 229335.
43 C. Feng, M. B. Faheem, J. Fu, Y. Xiao, C. Li and Y. Li, *ACS Catal.*, 2020, **10**, 4019–4047.
44 K. Zeng, X. Zheng, C. Li, J. Yan, J.-H. Tian, C. Jin, P. Strasser, R. Yang, K. Zeng, X. J. Zheng, C. Li, J. Yan, J. Tian, C. Jin, R. Z. Yang and P. Strasser, *Adv. Funct. Mater.*, 2020, **30**, 2000503.
45 H. Dau, C. Limberg, T. Reier, M. Risch, S. Roggan and P. Strasser, *ChemCatChem*, 2010, **2**, 724–761.
46 F. Lu, M. Zhou, Y. Zhou, X. Zeng, F. Lu, M. Zhou, Y. Zhou and X. Zeng, *Small*, 2017, **13**, 1701931.
47 H. Dau, C. Limberg, T. Reier, M. Risch, S. Roggan and P. Strasser, *ChemCatChem*, 2010, **2**, 724–761.
48 R. Gao and D. Yan, *Adv. Energy Mater.*, 2020, **10**, 1900954.
49 L. Trotochaud, S. L. Young, J. K. Ranney and S. W. Boettcher, *J. Am. Chem. Soc.*, 2014, **136**, 6744–6753.
50 D. Friebel, M. W. Louie, M. Bajdich, K. E. Sanwald, Y. Cai, A. M. Wise, M.-J. Cheng, D. Sokaras, T.-C. Weng, R. Alonso-Mori, R. C. Davis, J. R. Bargar, J. K. Nørskov, A. Nilsson and A. T. Bell, *J. Am. Chem. Soc.*, 2015, **137**, 1305–1313.
51 J. Jiang, F. Sun, S. Zhou, W. Hu, H. Zhang, J. Dong, Z. Jiang, J. Zhao, J. Li, W. Yan and M. Wang, *Nat. Commun.*, 2018, **9**, 2885.
52 J. Chen, M. Gu, S. Liu, T. Sheng and X. Zhang, *ACS Appl. Mater. Interfaces*, 2021, **13**, 16210–16217.
53 R. Wei, X. Bu, W. Gao, R. A. B. Villaos, G. MacAm, Z. Q. Huang, C. Lan, F. C. Chuang, Y. Qu and J. C. Ho, *ACS Appl. Mater. Interfaces*, 2019, **11**, 33012–33021.
54 T. Kang, K. Kim, M. Kim and J. Kim, *Chem. Eng. J.*, 2021, **418**, 129403.
55 P. Babar, A. Lokhande, V. Karade, B. Pawar, M. G. Gang, S. Pawar and J. H. Kim, *ACS Sustainable Chem. Eng.*, 2019, **7**, 10035–10043.
56 D. A. Corrigan, *J. Electrochem. Soc.*, 1987, **134**, 377.
57 G. Młynarek, M. Paszkiewicz and A. Radniecka, *J. Appl. Electrochem.*, 1984, **14**, 145–149.

58 L. Trotochaud, J. K. Ranney, K. N. Williams and S. W. Boettcher, *J. Am. Chem. Soc.*, 2012, **134**, 17253–17261.
59 Z. Sun, A. Curto, J. Rodríguez-Fernández, Z. Wang, A. Parikh, J. Fester, M. Dong, A. Vojvodic and J. V. Lauritsen, *ACS Nano*, 2021, **15**, 18226–18236.
60 U. I. Kramm, L. Ni and S. Wagner, *Adv. Mater.*, 2019, **31**, 1805623.
61 J. Y. C. Chen, L. Dang, H. Liang, W. Bi, J. B. Gerken, S. Jin, E. E. Alp and S. S. Stahl, *J. Am. Chem. Soc.*, 2015, **137**, 15090–15093.
62 M. Görlin, P. Chernev, J. F. de Araújo, T. Reier, S. Dresp, B. Paul, R. Krähnert, H. Dau and P. Strasser, *J. Am. Chem. Soc.*, 2016, **138**, 5603–5614.
63 G. Fu, X. Wen, S. Xi, Z. Chen, W. Li, J.-Y. Zhang, A. Tadich, R. Wu, D.-C. Qi, Y. Du, J. Cheng and K. H. L. Zhang, *Chem. Mater.*, 2018, **31**, 419–428.
64 Q. Li, X. Wang, K. Tang, M. Wang, C. Wang and C. Yan, *ACS Nano*, 2017, **11**, 12230–12239.
65 Y. Wang, C. Xie, Z. Zhang, D. Liu, R. Chen and S. Wang, *Adv. Funct. Mater.*, 2018, **28**, 1703363.
66 S. Niu, W.-J. Jiang, Z. Wei, T. Tang, J. Ma, J.-S. Hu and L.-J. Wan, *J. Am. Chem. Soc.*, 2019, **141**, 7005–7013.
67 S. Han, S. Liu, R. Wang, X. Liu, L. Bai and Z. He, *ACS Appl. Mater. Interfaces*, 2017, **9**, 17186–17194.
68 X. Wu and K. Scott, *J. Mater. Chem.*, 2011, **21**, 12344–12351.
69 B. Chi, H. Lin and J. Li, *Int. J. Hydrogen Energy*, 2008, **33**, 4763–4768.
70 T. W. Kim, M. A. Woo, M. Regis and K.-S. Choi, *J. Phys. Chem. Lett.*, 2014, **5**, 2370–2374.
71 P. W. Menezes, A. Indra, A. Bergmann, P. Chernev, C. Walter, H. Dau, P. Strasser and M. Driess, *J. Mater. Chem. A*, 2016, **4**, 10014–10022.
72 Y. Zhou, S. Sun, J. Song, S. Xi, B. Chen, Y. Du, A. C. Fisher, F. Cheng, X. Wang, H. Zhang and Z. J. Xu, *Adv. Mater.*, 2018, **30**, 1802912.
73 Y. Zhang, C. Wu, H. Jiang, Y. Lin, H. Liu, Q. He, S. Chen, T. Duan, L. Song, Y. Zhang, C. Wu, H. Jiang, Y. Lin, H. Liu, Q. He, S. Chen, L. Song and T. Duan, *Adv. Mater.*, 2018, **30**, 1707522.
74 S. K. Bikkarolla and P. Papakonstantinou, *J. Power Sources*, 2015, **281**, 243–251.
75 Y. Peng, H. Hajiyani and R. Pentcheva, *ACS Catal.*, 2021, **11**, 5601–5613.
76 M. Cui, X. Ding, X. Huang, Z. Shen, T.-L. Lee, F. E. Oropeza, J. P. Hofmann, E. J. M. Hensen and K. H. L. Zhang, *Chem. Mater.*, 2019, **31**, 7618–7625.
77 X. Wu, T. Zhang, J. Wei, P. Feng, X. Yan and Y. Tang, *Nano Res.*, 2020, **13**, 2130–2135.
78 B. Guo, R. Ma, Z. Li, J. Luo, M. Yang and J. Wang, *Mater. Chem. Front.*, 2020, **4**, 1390–1396.
79 Y. Song, J. Cheng, J. Liu, Q. Ye, X. Gao, J. Lu and Y. Cheng, *Appl. Catal., B*, 2021, **298**, 120488.
80 D. C. Nguyen, T. L. Luyen Doan, S. Prabhakaran, D. T. Tran, D. H. Kim, J. H. Lee and N. H. Kim, *Nano Energy*, 2021, **82**, 105750.
81 J. Qi, H. Wang, J. Lin, C. Li, X. Si, J. Cao, Z. Zhong and J. Feng, *J. Colloid Interface Sci.*, 2019, **557**, 28–33.
82 H. Sun, Y. Zhao, K. Mølhave, M. Zhang and J. Zhang, *Nanoscale*, 2017, **9**, 14431–14441.
83 K. L. Yan, X. Shang, Z. Z. Liu, B. Dong, S. S. Lu, J. Q. Chi, W. K. Gao, Y. M. Chai and C. G. Liu, *Int. J. Hydrogen Energy*, 2017, **42**, 24150–24158.
84 Q. Li, S. Li, O. Ajouyed, C. Chen, Y. Zhou, C. Li, S. Niu, H. Yi, J. Huo and S. Wang, *J. Alloys Compd.*, 2020, **816**, 152610.
85 L. Xu, Q. Jiang, Z. Xiao, X. Li, J. Huo, S. Wang and L. Dai, *Angew. Chem., Int. Ed.*, 2016, **55**, 5277–5281.
86 J. Sun, N. Guo, Z. Shao, K. Huang, Y. Li, F. He and Q. Wang, *Adv. Energy Mater.*, 2018, **8**, 1800980.
87 M. Xing, W. Fang, M. Nasir, Y. Ma, J. Zhang and M. Anpo, *J. Catal.*, 2013, **297**, 236–243.
88 Y. Wang, T. Zhou, K. Jiang, P. Da, Z. Peng, J. Tang, B. Kong, W.-B. Cai, Z. Yang and G. Zheng, *Adv. Energy Mater.*, 2014, **4**, 1400696.
89 Z. Cai, Y. Bi, E. Hu, W. Liu, N. Dwarica, Y. Tian, X. Li, Y. Kuang, Y. Li, X.-Q. Yang, H. Wang and X. Sun, *Adv. Energy Mater.*, 2018, **8**, 1701694.
90 S. Peng, F. Gong, L. Li, D. Yu, D. Ji, T. Zhang, Z. Hu, Z. Zhang, S. Chou, Y. Du and S. Ramakrishna, *J. Am. Chem. Soc.*, 2018, **140**, 13644–13653.
91 M. Asnavandi, Y. Yin, Y. Li, C. Sun and C. Zhao, *ACS Energy Lett.*, 2018, **3**, 1515–1520.
92 L. Zhuang, L. Ge, Y. Yang, M. Li, Y. Jia, X. Yao and Z. Zhu, *Adv. Mater.*, 2017, **29**, 1606793.
93 J. Bao, X. Zhang, B. Fan, J. Zhang, M. Zhou, W. Yang, X. Hu, H. Wang, B. Pan and Y. Xie, *Angew. Chem., Int. Ed.*, 2015, **54**, 7399–7404.
94 F. Cheng, T. Zhang, Y. Zhang, J. Du, X. Han and J. Chen, *Angew. Chem., Int. Ed.*, 2013, **52**, 2474–2477.
95 X. Miao, L. Wu, Y. Lin, X. Yuan, J. Zhao, W. Yan, S. Zhou and L. Shi, *Chem. Commun.*, 2019, **55**, 1442–1445.
96 Z. Wang, Y. Zhang, E. C. Neyts, X. Cao, X. Zhang, B. W.-L. Jang and C. Liu, *ACS Catal.*, 2018, **8**, 2093–2110.
97 M. X. Lin, F. Shao, S. Weng, S. Xiong, S. Liu, S. Jiang, Y. Xu, Y. Jiao and J. Chen, *Electrochim. Acta*, 2021, **378**, 138147.
98 R. Liu, Y. Wang, D. Liu, Y. Zou and S. Wang, *Adv. Mater.*, 2017, **29**, 1701546.
99 H. Chen, Q. Zhao, L. Gao, J. Ran and Y. Hou, *ACS Sustainable Chem. Eng.*, 2019, **7**, 4247–4254.
100 L. Ma, S. Chen, Z. Pei, H. Li, Z. Wang, Z. Liu, Z. Tang, J. A. Zapien and C. Zhi, *ACS Nano*, 2018, **12**, 8597–8605.
101 L. Xu, Z. Wang, J. Wang, Z. Xiao, X. Huang, Z. Liu and S. Wang, *Nanotechnology*, 2017, **28**, 165402.
102 K. Zeng, W. Li, Y. Zhou, Z. Sun, C. Lu, J. Yan, J. H. Choi and R. Yang, *Chem. Eng. J.*, 2021, **421**, 127831.
103 Y. Lu, A. Ma, Y. Yu, R. Tan, C. Liu, P. Zhang, D. Liu and J. Gui, *ACS Sustainable Chem. Eng.*, 2018, **7**, 2906–2910.
104 Y. Zhang, B. Ouyang, J. Xu, G. Jia, S. Chen, R. S. Rawat and H. J. Fan, *Angew. Chem., Int. Ed.*, 2016, **55**, 8670–8674.
105 Y. Liu, M. Zhang, D. Hu, R. Li, K. Hu and K. Yan, *ACS Appl. Energy Mater.*, 2019, **2**, 1162–1168.
106 C. Lei, W. Li, G. Wang, L. Zhuang, J. Lu and L. Xiao, *Chem. Res. Chin. Univ.*, 2021 3722021, **37**, 293–297.
107 Y. Zhu, X. Zhong, S. Jin, H. Chen, Z. He, Q. Liu and Y. Chen, *J. Mater. Chem. A*, 2020, **8**, 10957–10965.

108 S. Jin, Y. Zhu, Z. He, H. Chen, X. Liu, F. Li, J. Liu, M. Liu and Y. Chen, *Int. J. Hydrogen Energy*, 2020, **45**, 424–432.
109 X. Wang, L. Zhuang, Y. Jia, H. Liu, X. Yan, L. Zhang, D. Yang, Z. Zhu and X. Yao, *Angew. Chem., Int. Ed.*, 2018, **57**, 16421–16425.
110 W. Xu, Y. Bai and Y. Yin, *Adv. Mater.*, 2018, **30**, 1802091.
111 W. Xu, F. Lyu, Y. Bai, A. Gao, J. Feng, Z. Cai and Y. Yin, *Nano Energy*, 2018, **43**, 110–116.
112 G. R. Zhang and B. J. M. Etzold, *J. Energy Chem.*, 2016, **25**, 199–207.
113 H. Liu, Y. Liu and J. Li, *Phys. Chem. Chem. Phys.*, 2010, **12**, 1685–1697.
114 J. Sun, N. Guo, Z. Shao, K. Huang, Y. Li, F. He and Q. Wang, *Adv. Energy Mater.*, 2018, **8**, 1800980.
115 A. A. Chaugule, V. S. Mane, H. A. Bandal, H. Kim and A. S. Kumbhar, *ACS Sustainable Chem. Eng.*, 2019, **7**, 14889–14898.
116 I. S. Cho, M. Logar, C. H. Lee, L. Cai, F. B. Prinz and X. Zheng, *Nano Lett.*, 2013, **14**, 24–31.
117 D. Zhou, X. Xiong, Z. Cai, N. Han, Y. Jia, Q. Xie, X. Duan, T. Xie, X. Zheng, X. Sun and X. Duan, *Small Methods*, 2018, **2**, 1800083.
118 C. Meng, M. Lin, X. Sun, X. Chen, X. Chen, X. Du and Y. Zhou, *Chem. Commun.*, 2019, **55**, 2904–2907.
119 Y. Zhou, C.-K. Dong, L. Han, J. Yang and X.-W. Du, *ACS Catal.*, 2016, **6**, 6699–6703.
120 C. Dong, Z.-W. Liu, J.-Y. Liu, W.-C. Wang, L. Cui, R.-C. Luo, H.-L. Guo, X.-L. Zheng, S.-Z. Qiao, X.-W. Du and J. Yang, *Small*, 2017, **13**, 1603903.
121 J. Lai, W. Niu, R. Luque and G. Xu, *Nano Today*, 2015, **10**, 240–267.
122 M. Zhou, C. Li and J. Fang, *Chem. Rev.*, 2020, **121**, 736–795.
123 F. Pang, Z. Wang, K. Zhang, J. He, W. Zhang, C. Guo and Y. Ding, *Nano Energy*, 2019, **58**, 834–841.
124 W. Luc, C. Collins, S. Wang, H. Xin, K. He, Y. Kang and F. Jiao, *J. Am. Chem. Soc.*, 2017, **139**, 1885–1893.
125 T. Reier, Z. Pawolek, S. Cherevko, M. Bruns, T. Jones, D. Teschner, S. Selve, A. Bergmann, H. N. Nong, R. Schlögl, K. J. J. Mayrhofer and P. Strasser, *J. Am. Chem. Soc.*, 2015, **137**, 13031–13040.
126 J. Lim, S. Yang, C. Kim, C.-W. Roh, Y. Kwon, Y.-T. Kim and H. Lee, *Chem. Commun.*, 2016, **52**, 5641–5644.
127 J. Feng, F. Lv, W. Zhang, P. Li, K. Wang, C. Yang, B. Wang, Y. Yang, J. Zhou, F. Lin, G.-C. Wang and S. Guo, *Adv. Mater.*, 2017, **29**, 1703798.
128 Y. Pi, Q. Shao, P. Wang, J. Guo and X. Huang, *Adv. Funct. Mater.*, 2017, **27**, 1700886.
129 F. Lv, J. Feng, K. Wang, Z. Dou, W. Zhang, J. Zhou, C. Yang, M. Luo, Y. Yang, Y. Li, P. Gao and S. Guo, *ACS Cent. Sci.*, 2018, **4**, 1244–1252.
130 X. Chen, M. Xu, S. Li, C. Li, X. Sun, S. Mu and J. Yu, *Adv. Mater. Interfaces*, 2020, **7**, 2001145.
131 S. Zhang, X. Zhang, X. Shi, F. Zhou, R. Wang and X. Li, *J. Energy Chem.*, 2020, **49**, 166–173.
132 Q. Yao, B. Huang, N. Zhang, M. Sun, Q. Shao and X. Huang, *Angew. Chem., Int. Ed.*, 2019, **58**, 13983–13988.
133 Q. Yang, P. Jin, B. Liu, L. Zhao, J. Cai, W. Zhan, S. Zuo, J. Zhang and F. Lai, *J. Mater. Chem. A*, 2020, **8**, 9049–9057.
134 T. T. H. Hoang and A. A. Gewirth, *ACS Catal.*, 2016, **6**, 1159–1164.
135 F. Shen, Y. Wang, G. Qian, W. Chen, W. Jiang, L. Luo and S. Yin, *Appl. Catal., B*, 2020, **278**, 119327.
136 C. Wang, H. Yang, Y. Zhang and Q. Wang, *Angew. Chem., Int. Ed.*, 2019, **58**, 6099–6103.
137 K. Liu, C. Zhang, Y. Sun, G. Zhang, X. Shen, F. Zou, H. Zhang, Z. Wu, E. C. Wegener, C. J. Taubert, J. T. Miller, Z. Peng and Y. Zhu, *ACS Nano*, 2017, **12**, 158–167.
138 L. Lv, Z. Li, K. H. Xue, Y. Ruan, X. Ao, H. Wan, X. Miao, B. Zhang, J. Jiang, C. Wang and K. Ostrikov, *Nano Energy*, 2018, **47**, 275–284.
139 M. Y. Gao, C. Yang, Q. B. Zhang, J. R. Zeng, X. T. Li, Y. X. Hua, C. Y. Xu and P. Dong, *J. Mater. Chem. A*, 2017, **5**, 5797–5805.
140 T. Zhang, X. Liu, X. Cui, M. Chen, S. Liu and B. Geng, *Adv. Mater. Interfaces*, 2018, **5**, 1800359.
141 J. Yang, Q. Shao, B. Huang, M. Sun and X. Huang, *iScience*, 2019, **11**, 492–504.
142 W. Cai, R. Chen, H. Yang, H. B. Tao, H.-Y. Wang, J. Gao, W. Liu, S. Liu, S.-F. Hung and B. Liu, *Nano Lett.*, 2020, **20**, 4278–4285.
143 D. Zhao, Y. Pi, Q. Shao, Y. Feng, Y. Zhang and X. Huang, *ACS Nano*, 2018, **12**, 6245–6251.
144 P. Zhai, Y. Zhang, Y. Wu, J. Gao, B. Zhang, S. Cao, Y. Zhang, Z. Li, L. Sun and J. Hou, *Nat. Commun.*, 2020, **11**, 5462.
145 Y. Liu, Y. Xing, S. Xu, Y. Lu, S. Sun and D. Jiang, *Chem. Eng. J.*, 2021, 133240.
146 Y. Li, J. Yin, L. An, M. Lu, K. Sun, Y.-Q. Zhao, D. Gao, F. Cheng, P. Xi, Y. Li, J. Yin, L. An, M. Lu, K. Sun, Y. Zhao, D. Gao, P. Xi and F. Cheng, *Small*, 2018, **14**, 1801070.
147 J. Zhang, T. Wang, D. Pohl, B. Rellinghaus, R. Dong, S. Liu, X. Zhuang and X. Feng, *Angew. Chem.*, 2016, **128**, 6814–6819.
148 Z. Niu, C. Qiu, J. Jiang and L. Ai, *ACS Sustainable Chem. Eng.*, 2019, **7**, 2335–2342.
149 Y. Gu, S. Chen, J. Ren, Y. A. Jia, C. Chen, S. Komarneni, D. Yang and X. Yao, *ACS Nano*, 2018, **12**, 245–253.
150 Y. Bu, H. Jang, O. Gwon, S. H. Kim, S. H. Joo, G. Nam, S. Kim, Y. Qin, Q. Zhong, S. K. Kwak, J. Cho and G. Kim, *J. Mater. Chem. A*, 2019, **7**, 2048–2054.
151 M. Tahir, N. Mahmood, X. Zhang, T. Mahmood, F. K. Butt, I. Aslam, F. Idrees, S. Khalid, I. Shakir, Y. Yan, J. Zou, C. Cao, Y. Hou and S.-V. Berlin, *Nano Res.*, 2015, **8**, 3725–3736.
152 C. Huang, T. Ouyang, Y. Zou, N. Li and Z. Q. Liu, *J. Mater. Chem. A*, 2018, **6**, 7420–7427.
153 F. Davodi, E. Mühlhausen, M. Tavakkoli, J. Sainio, H. Jiang, B. Gökce, G. Marzun and T. Kallio, *ACS Appl. Mater. Interfaces*, 2018, **10**, 31300–31311.
154 X. Bai, Q. Wang and J. Guan, *ACS Appl. Nano Mater.*, 2021, **4**, 12663–12671.

155 D. Ye, T. Wu, H. Cao, Y. Wang, B. Liu, S. Zhang and J. Kong, *RSC Adv.*, 2015, **5**, 26710–26715.
156 L. Truong, S. K. Jerng, S. B. Roy, J. H. Jeon, K. Kim, K. Akbar, Y. Yi and S. H. Chun, *ACS Sustainable Chem. Eng.*, 2019, **7**, 4625–4630.
157 M. S. Ahmed, B. Choi and Y. B. Kim, *Sci. Rep.*, 2018, **8**, 1–10.
158 H. Liu, C. Y. Xu, Y. Du, F. X. Ma, Y. Li, J. Yu and L. Zhen, *Sci. Rep.*, 2019, **9**, 1–10.
159 F. Li, H. Ai, D. Liu, K. H. Lo and H. Pan, *J. Mater. Chem. A*, 2021, **9**, 17749–17759.
160 M. Luo and S. Guo, *Nat. Rev. Mater.*, 2017, **2**, 17059.
161 K. A. Stoerzinger, W. Seok Choi, H. Jeen, H. N. Lee and Y. Shao-Horn, *J. Phys. Chem. Lett.*, 2015, **6**, 487–492.
162 J. R. Petrie, V. R. Cooper, J. W. Freeland, T. L. Meyer, Z. Zhang, D. A. Lutterman and H. N. Lee, *J. Am. Chem. Soc.*, 2016, **138**, 2488–2491.
163 B. You, M. T. Tang, C. Tsai, F. Abild-Pedersen, X. Zheng and H. Li, *Adv. Mater.*, 2019, **31**, 1807001.
164 X. Yang, Y. Wang, X. Tong, N. Yang, X. Yang, Y. Wang, X. Tong and N. Yang, *Adv. Energy Mater.*, 2022, **12**, 2102261.
165 A. Kushima, S. Yip and B. Yildiz, *Phys. Rev. B: Condens. Matter Mater. Phys.*, 2010, **82**, 115435.
166 E. E. Benson, M. A. Ha, B. A. Gregg, J. van de Lagemaat, N. R. Neale and D. Svedruzic, *Sci. Rep.*, 2019, **9**, 1–8.
167 J. R. Petrie, H. Jeen, S. C. Barron, T. L. Meyer and H. N. Lee, *J. Am. Chem. Soc.*, 2016, **138**, 7252–7255.
168 D. Zhou, S. Wang, Y. Jia, X. Xiong, H. Yang, S. Liu, J. Tang, J. Zhang, D. Liu, L. Zheng, Y. Kuang, X. Sun and B. Liu, *Angew. Chem.*, 2019, **131**, 746–750.
169 Y. Wang, X. Li, M. Zhang, Y. Zhou, D. Rao, C. Zhong, J. Zhang, X. Han, W. Hu, Y. Zhang, K. Zaghib, Y. Wang and Y. Deng, *Adv. Mater.*, 2020, **32**, 2000231.
170 Q. Ji, Y. Kong, C. Wang, H. Tan, H. Duan, W. Hu, G. Li, Y. Lu, N. Li, Y. Wang, J. Tian, Z. Qi, Z. Sun, F. Hu and W. Yan, *ACS Catal.*, 2020, **10**, 5691–5697.
171 X. Yu, Z. Sun, Z. Yan, B. Xiang, X. Liu and P. Du, *J. Mater. Chem. A*, 2014, **2**, 20823–20831.
172 Y. Hou, M. Qiu, M. G. Kim, P. Liu, G. Nam, T. Zhang, X. Zhuang, B. Yang, J. Cho, M. Chen, C. Yuan, L. Lei and X. Feng, *Nat. Commun.*, 2019, **10**, 1–9.
173 Y. Jia, L. Zhang, A. Du, G. Gao, J. Chen, X. Yan, C. L. Brown, X. Yao, Y. Jia, L. Z. Zhang, X. C. Yan, X. D. Yao, C. L. Brown, A. J. Du, G. P. Gao and J. Chen, *Adv. Mater.*, 2016, **28**, 9532–9538.
174 Y. Zhou, W. Zhang, J. Hu, D. Li, X. Yin and Q. Gao, *ACS Sustainable Chem. Eng.*, 2021, **9**, 7390–7399.
175 R. I. Sayler, B. M. Hunter, W. Fu, H. B. Gray and R. D. Britt, *J. Am. Chem. Soc.*, 2020, **142**, 1838–1845.
176 Q. Lihua, H. Xiao, K. Chi, H. Yin, X. Zhou, P. Lei, P. Liu, J. Fang, X. Li, S. Yuan, Z. Zhang, Y. Su, J. Guo, L. Qian, H. Xiao, H. Yin, X. Zhou, S. Yuan, L. Qian, K. Chi, P. Lei, P. Liu, J. Guo, cn J. Fang, X. Li, Z. Zhang and Y. Su, *Energy Environ. Mater.*, 2022, e12495.
177 E. Fabbri, D. F. Abbott, M. Nachtegaal and T. J. Schmidt, *Curr. Opin. Electrochem.*, 2017, **5**, 20–26.
178 Y. Zhao, X. Zhang, X. Jia, G. I. N. Waterhouse, R. Shi, X. Zhang, F. Zhan, Y. Tao, L. Z. Wu, C. H. Tung, D. O'Hare and T. Zhang, *Adv. Energy Mater.*, 2018, **8**, 1703585.
179 C. Liu, Y. Han, L. Yao, L. Liang, J. He, Q. Hao, J. Zhang, Y. Li, H. Liu, C. C. Liu, Y. Han, L. M. Liang, J. Y. He, Q. Y. Hao, J. Zhang, Y. Li, H. Liu and L. B. Yao, *Small*, 2021, **17**, 2007334.
180 S. Liu, H. Cheng, K. Xu, H. Ding, J. Zhou, B. Liu, W. Chu, C. Wu and Y. Xie, *ACS Energy Lett.*, 2019, **4**, 423–429.
181 X. Qiao, H. Kang, Y. Li, K. Cui, X. Jia, X. Wu and W. Qin, *Appl. Catal., B*, 2022, **305**, 121034.
182 L. Wu, T. Guo and T. Li, *iScience*, 2021, **24**, 102398.
183 Y. F. Li, *ChemSusChem*, 2019, **12**, 1846–1857.
184 W. Liu, L. Yu, R. Yin, X. Xu, J. Feng, X. Jiang, D. Zheng, X. Gao, X. Gao, W. Que, P. Ruan, F. Wu, W. Shi, X. Cao, W. Liu, L. Yu, R. Yin, X. Xu, J. Feng, X. Jiang, D. Zheng, X. Gao, W. Que, P. Ruan, F. Wu, X. Cao and W. Shi, *Small*, 2020, **16**, 1906775.
185 L. Wang, Q. Zhou, Z. Pu, Q. Zhang, X. Mu, H. Jing, S. Liu, C. Chen and S. Mu, *Nano Energy*, 2018, **53**, 270–276.
186 D. Wang, Q. Li, C. Han, Q. Lu, Z. Xing and X. Yang, *Nat. Commun.*, 2019, **10**, 3899.
187 H. Park, J. W. Bae, T. H. Lee, I. J. Park, C. Kim, M. G. Lee, S. A. Lee, J. W. Yang, M. J. Choi, S. H. Hong, S. Y. Kim, S. H. Ahn, J. Y. Kim, H. S. Kim and H. W. Jang, *Small*, 2022, **18**, 2105611.
188 H. Liu, H. Qin, J. Kang, L. Ma, G. Chen, Q. Huang, Z. Zhang, E. Liu, H. Lu, J. Li and N. Zhao, *Chem. Eng. J.*, 2022, **435**, 134898.
189 Z. Chen, W. Wang, S. Huang, P. Ning, Y. Wu, C. Gao, T. T. Le, J. Zai, Y. Jiang, Z. Hu and X. Qian, *Nanoscale*, 2019, **12**, 326–335.
190 Q. Wu, A. Dong, C. Yang, L. Ye, L. Zhao and Q. Jiang, *Chem. Eng. J.*, 2021, **413**, 127482.
191 Y. Sun, T. Liu, Z. Li, A. Meng, G. Li, L. Wang and S. Li, *Chem. Eng. J.*, 2022, **433**, 133684.
192 J. Liu, G. Qian, T. Yu, J. Chen, C. Zhu, Y. Li, J. He, L. Luo and S. Yin, *Chem. Eng. J.*, 2022, **431**, 134247.
193 F. Nie, Z. Li, X. Dai, X. Yin, Y. Gan, Z. Yang, B. Wu, Z. Ren, Y. Cao and W. Song, *Chem. Eng. J.*, 2022, **431**, 134080.
194 P. Babar, K. Patil, J. Mahmood, S. jin Kim, J. H. Kim and C. T. Yavuz, *Cell Rep. Phys. Sci.*, 2022, **3**, 100762.
195 L. Sun, Z. Dai, L. Zhong, Y. Zhao, Y. Cheng, S. Chong, G. Chen, C. Yan, X. Zhang, H. Tan, L. Zhang, K. N. Dinh, S. Li, F. Ma and Q. Yan, *Appl. Catal., B*, 2021, **297**, 120477.
196 M. Han, S. Li, C. Li, J. Wu, J. Han, N. Wang, Y. Liu and H. Liang, *J. Alloys Compd.*, 2020, **844**, 156094.
197 X. Gao, Y. Zhou, Y. Tan, S. Liu, Z. Cheng and Z. Shen, *Phys. Chem. Chem. Phys.*, 2020, **22**, 2457–2465.
198 H. Liu, M. Jin, D. Zhan, J. Wang, X. Cai, Y. Qiu and L. Lai, *Appl. Catal., B*, 2020, **272**, 118951.
199 Z. Li, H. Jang, D. Qin, X. Jiang, X. Ji, M. G. Kim, L. Zhang, X. Liu and J. Cho, *J. Mater. Chem. A*, 2021, **9**, 4036–4043.
200 Z. Hou, Z. Sun, C. Cui, D. Zhu, Y. Yang and T. Zhang, *Adv. Funct. Mater.*, 2022, 2110572.
201 W. Cheng, X. Zhao, H. Su, F. Tang, W. Che, H. Zhang and Q. Liu, *Nat. Energy*, 2019, **4**, 115–122.